J. Fluid Mech. (1990), *vol.* 210, *pp.* 223–261
Printed in Great Britain

The stability of elliptical vortices in an external straining flow

By DAVID G. DRITSCHEL
Department of Applied Mathematics and Theoretical Physics, University of Cambridge, Silver Street, Cambridge CB3 9EW, UK

(Received 28 October 1988 and in revised form 19 June 1989)

Subject to uniform strain, an elliptical patch of vorticity in an inviscid, incompressible, two-dimensional fluid generally rotates or nutates and extends or compresses while retaining a precisely elliptical shape (the Kida solutions). This result is of interest because the uniform strain idealizes the leading-order distortional influence of distant vortices in a flow with many vortices. Because of the unsteady motion of the distant vortices, both the strain rate and the rotation rate of the strain axes typically vary with time. In the special case that the strain rate and rotation rate are steady, and when the strain rate is not too large, periodic motion of an elliptical vortex is possible. Larger strain rates lead to indefinite extension of the vortex.

Uniform strain, however, only approximately mimics the effect of distant vortices. The local variations in the strain field around a vortex disturb the vortex, preventing it from retaining a simple, elliptical shape. These disturbances may amplify because of instabilities. In this paper, we examine the stability of periodic elliptical motion to small boundary disturbances, for the case of steady, uniform strain and rotation rate, first by linear Floquet theory and then by direct, high-resolution, nonlinear numerical integrations. It is discovered that a significant portion of the periodic solutions are linearly unstable. Instability can occur even when the strain rate is arbitrarily small and the basic motion arbitrarily close to circular. Extended nonlinear calculations exhibit recurrence, in some cases, and attrition of the vortex by repeated wave amplification, steepening, and breaking in others.

1. Introduction

In an inviscid, incompressible, two-dimensional fluid, a patch of uniform vorticity that is exactly elliptical remains elliptical when subjected to an external strain and rotation of the form

$$u_s = \gamma(t)\,x - \Omega(t)\,y, \quad v_s = \Omega(t)\,x - \gamma(t)\,y, \tag{1}$$

where the strain rate, γ, and the rotation rate, Ω, are arbitrary functions of time t (Kida 1981). In general, the aspect ratio λ and orientation ϕ of the ellipse (see figure 1) vary with time, in accordance with

$$\frac{\mathrm{d}\lambda}{\mathrm{d}t} = 2\gamma\lambda\cos 2\phi, \tag{2a}$$

$$\frac{\mathrm{d}\phi}{\mathrm{d}t} = \Omega + \frac{\omega\lambda}{(\lambda+1)^2} - \gamma\sin 2\phi\,\frac{\lambda^2+1}{\lambda^2-1}, \tag{2b}$$

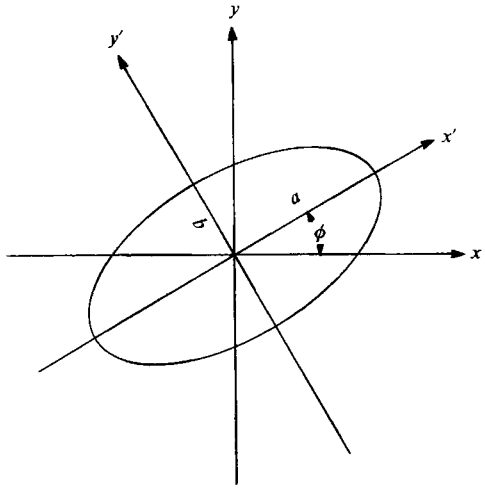

FIGURE 1. Sketch of the basic ellipse. The quantities $a(t)$ and $b(t)$ are the lengths of the semi-major and semi-minor axes respectively. The aspect ratio of the ellipse is defined as $\lambda = a/b$. Without loss of generality, $ab = 1$, and the vorticity of the fluid inside the ellipse exceeds that outside by unity ($\omega = 1$).

where ω, set to unity hereinafter, is the relative vorticity within the ellipse (relative, that is, to the uniform background value 2Ω).

This situation has interest not only in its own right but also as a possible idealization of the effects of distant vortices in an unsteady flow at very high Reynolds numbers populated by many vortices. Such flows, which are of fundamental interest in geophysical fluid dynamics, often show a tendency to become more and more inhomogeneous, with the development of widely separated, well-organized vortices from smaller scale structures (Fornberg 1977; Basdevant, Legras & Sadourny 1981; McWilliams 1984; Legras, Santangelo & Benzi 1988). At first, the small structures rapidly combine or coalesce to form a succession of larger vortices. The rate of coalescence slows substantially with the growth of the vortices and, at late times, the vortices rarely encounter one another. These observations suggest that it may be appropriate to study the dynamics of the flow in its late stages by considering just one vortex and approximating the local effects of the remaining vortices by the straining flow (1). Local departures from (1) will be assumed to be the source of disturbances to the vortex in question.

The simplest model of a vortex in a straining flow takes the vortex to be a uniform patch of vorticity. Of course, the realism of such a model might well be questioned; however, a separate study (Legras & Dritschel 1989) has examined the effects of the straining flow (1) on a vortex with distributed or non-uniform vorticity, and, briefly, it is found that strain strips away material from the periphery leaving the vortex with an exceedingly steep edge. A stripped vortex can retain some of its internal structure, that is to say a non-uniform profile of vorticity, but in some cases the stripping is so extensive that the remaining vorticity is practically uniform. It appears that strong vortices with long lifetimes encounter a wide variety of external straining conditions and thereby tend to acquire very steep edge gradients (at very high Reynolds numbers). It is noteworthy that significant stripping can be brought about by surprisingly weak strain fields. The upshot is that, at very high Reynolds numbers, the vortex patch may not be as severe an idealization as might be thought.

The motivation for the present study is the vortex patch's possible relevance as a

model of the final stages of the life of an isolated, extensively stripped vortex subject to external strain and rotation. It is shown that the behaviour described by the Kida solutions is radically altered by the presence of small disturbances, such as might be introduced by slight departures from uniformity of strain and rotation. This is because many such disturbances are unstable.

The concept of stability presupposes a steady, or periodic, basic flow. We choose the simplest such basic flow, namely the periodic Kida solutions, which are given by (2) for steady γ and Ω. (In fact certain periodic variations of γ and Ω also result in periodic solutions, but these are not considered here.) The effect of unsteady, aperiodic strain and rotation must be examined by alternative means. This is beyond the scope of the present paper, but a proposal concerning it is put forth in §5.

The properties of the Kida solutions are recalled briefly in §2. Linearized disturbance equations are derived next in §3, and shown to take a remarkably simple form. A Floquet analysis provides maps of the maximum growth rate as a function of the basic-solution parameters and the disturbance symmetry. Section 4 presents nonlinear calculations. These reveal the order in amplitude at which nonlinearity enters and incidentally check the linear Floquet analysis. Further nonlinear calculations push as deep as possible into the complex evolution of unstable vortices and disclose a recurring, disruptive sequence of events in which qualitatively different manifestations of instability appear.

2. The undisturbed system

For steady strain γ and rotation Ω, (2*a*) and (2*b*) can be combined and integrated once to yield a relationship between the aspect ratio λ and the orientation ϕ of the vortex at any time t:

$$\gamma \sin 2\phi = \frac{\lambda}{\lambda^2-1}\left[\log\frac{(\lambda+1)^2}{4\lambda}+c\right]+\frac{\lambda-1}{\lambda+1}\Omega. \tag{3}$$

The constant c is found upon specifying λ and ϕ at one instant of time, typically the initial time. However, it is more instructive to choose c in terms of λ and ϕ at the time when λ assumes its minimum value, say $\lambda = \lambda_0 \geqslant 1$. From (2*a*), it is clear that a minimum must occur when $\cos 2\phi = 0$ or $\sin 2\phi = \pm 1$ (except when $\lambda_0 = 1$ as noted below). Since all periodic solutions must have a minimum aspect ratio, it is sufficient to specify the four parameters γ, Ω, λ_0 and s, the sign of $\sin 2\phi$ when $\lambda = \lambda_0$. In terms of these parameters, the constant of integration of (3) has the form

$$c = \frac{\lambda_0-1}{\lambda_0}[(\lambda_0+1)\gamma s-(\lambda_0-1)\Omega]-\log\frac{(\lambda_0+1)^2}{4\lambda_0}. \tag{4}$$

Since γ and s appear only in the product γs, it is not only sufficient to consider $\gamma \geqslant 0$ and $s = \pm 1$, but a unique solution (λ, ϕ) then corresponds to each distinct choice of the four parameters.

When $\lambda_0 = 1$, $\lambda(t)$ can equal 1 only when $\sin 2\phi = 0$ (to keep the last term in (2*b*) well behaved). While $\dot{\lambda} \equiv \mathrm{d}\lambda/\mathrm{d}t \neq 0$ when $\lambda = 1$, the sign of $\cos 2\phi$ is abruptly reversed at the instant $\lambda = 1$ in order to keep $\lambda \geqslant 1$ throughout the evolution. This perhaps worrisome procedure is given a sound basis by introducing transformed variables X and Y in terms of which λ can be defined to be greater than or equal to 1. Let

$$X = (\lambda-\lambda^{-1})\cos 2\phi, \quad Y = (\lambda-\lambda^{-1})\sin 2\phi \tag{5a, b}$$

(cf. Melander, Zabusky & Styczek 1986). Then, the transformed equations of motions are

$$\dot{X} = -2Y(\Omega+\Omega_e)+\gamma R, \quad \dot{Y} = +2X(\Omega+\Omega_e), \quad R = (X^2+Y^2)^{\frac{1}{2}}, \qquad (6a, b, c)$$

where

$$\Omega_e = \frac{\lambda}{(\lambda+1)^2} \qquad (7)$$

is the rotation rate of a freely rotating (unforced) ellipse of aspect ratio

$$\lambda = (1+\tfrac{1}{4}R^2)^{\frac{1}{2}}+\tfrac{1}{2}R. \qquad (8)$$

Figure 2 shows the domain of periodic solutions for $\lambda_0 = 1$ and $\lambda_0 = 2$ ($s = \pm 1$). The domain always consists of two distinct regions in which the character of the solutions differs markedly. When $\lambda_0 = 1$, the solutions in the left region rotate clockwise ($\dot{\phi} < 0$) while those in the right rotate counter-clockwise ($\dot{\phi} > 0$). The dividing curve $\gamma_c(\Omega)$ defines the upper limit of the right region. Solutions just beneath this curve only just pass through $\phi = \frac{1}{4}\pi$, at which orientation the aspect ratio is greatest, taking an infinite amount of time to do so. Likewise, solutions along the upper limit of the left region, the line $\gamma = -\Omega$, take forever to pass through $\phi = -\frac{1}{4}\pi$, where the aspect ratio is not only greatest but infinite. Recall that positive values of Ω imply that the strain axes rotate in an opposite direction to the self-induced vortex rotation Ω_e; negative values imply just the opposite. Just above $\gamma_c(\Omega)$ and $\gamma = -\Omega$, periodic solutions yield to monotonically extending ones. The line $\gamma = -\Omega$ intersects $\gamma_c(\Omega)$ at the point $\Omega = \Omega_c = -0.074\,388\,318\ldots$, and from there, $\gamma_c(\Omega)$ defines the lower limit of the left region until $\Omega = -\frac{1}{4}(= -\Omega_e(1)$, see (7)). Solutions along $\gamma = 0$ simply retain their initial aspect ratio, that is $\lambda(t) = 1$.

For $\lambda_0 = 2$ and $s = +1$, or for vortices oriented NE–SW at minimum aspect ratio, the domain of solutions differs qualitatively from that for $\lambda_0 = 1$ in only two respects. First, a forbidden region appears in the sector bounded by the lines $\gamma = 0$ and $\gamma = \bar{\gamma}(\Omega)$,

$$\bar{\gamma} = \frac{\lambda_0^2-1}{\lambda_0^2+1}(\Omega-\Omega_0), \qquad (9)$$

with vertex at

$$\Omega_0 = -\Omega_e(\lambda_0) = -\frac{\lambda_0}{(\lambda_0+1)^2}. \qquad (10)$$

Periodic solutions do exist in the forbidden region, only they do not satisfy $\lambda(t) \geqslant \lambda_0$ (in fact $\lambda(t) \leqslant \lambda_0$). Second, the right region contains nutating rather than counter-clockwise rotating solutions, and it exists only for $\Omega \geqslant \Omega_1$ where

$$\Omega_1 = \Omega_0+\left(\frac{\lambda_0-1}{\lambda_0+1}\right)^2\left(\frac{\lambda_0^2+1}{4\lambda_0}\right). \qquad (11)$$

For these solutions, the orientation angle ϕ oscillates about $\phi = \frac{1}{4}\pi$ in such a way that $\dot{\phi} < 0$ when $\lambda = \lambda_0$, and $\dot{\phi} > 0$ when $\lambda = \lambda_{\max}$. Just beneath the curve $\gamma = \gamma_c^+(\Omega)$, the maximum angular swing, $\phi_{\max}-\phi_{\min}$, nears π, while just above the line $\bar{\gamma}(\Omega)$, it nears zero. As Ω approaches Ω_1, the frequency of nutation for a solution arbitrarily near this line tends to zero and, in fact, becomes imaginary in the range $\Omega_0 < \Omega < \Omega_1$ (see §3 below). The line $\bar{\gamma}$ itself defines stationary solutions, discovered earlier by Moore & Saffman (1971).

For $\lambda_0 = 2$ and $s = -1$, or for vortices oriented NW–SE at minimum aspect ratio, a forbidden region appears on the left, between the lines $\gamma = 0$ and $-\bar{\gamma}(\Omega)$, stacked on top of which is a region of nutating solutions. The sense of nutation is simply

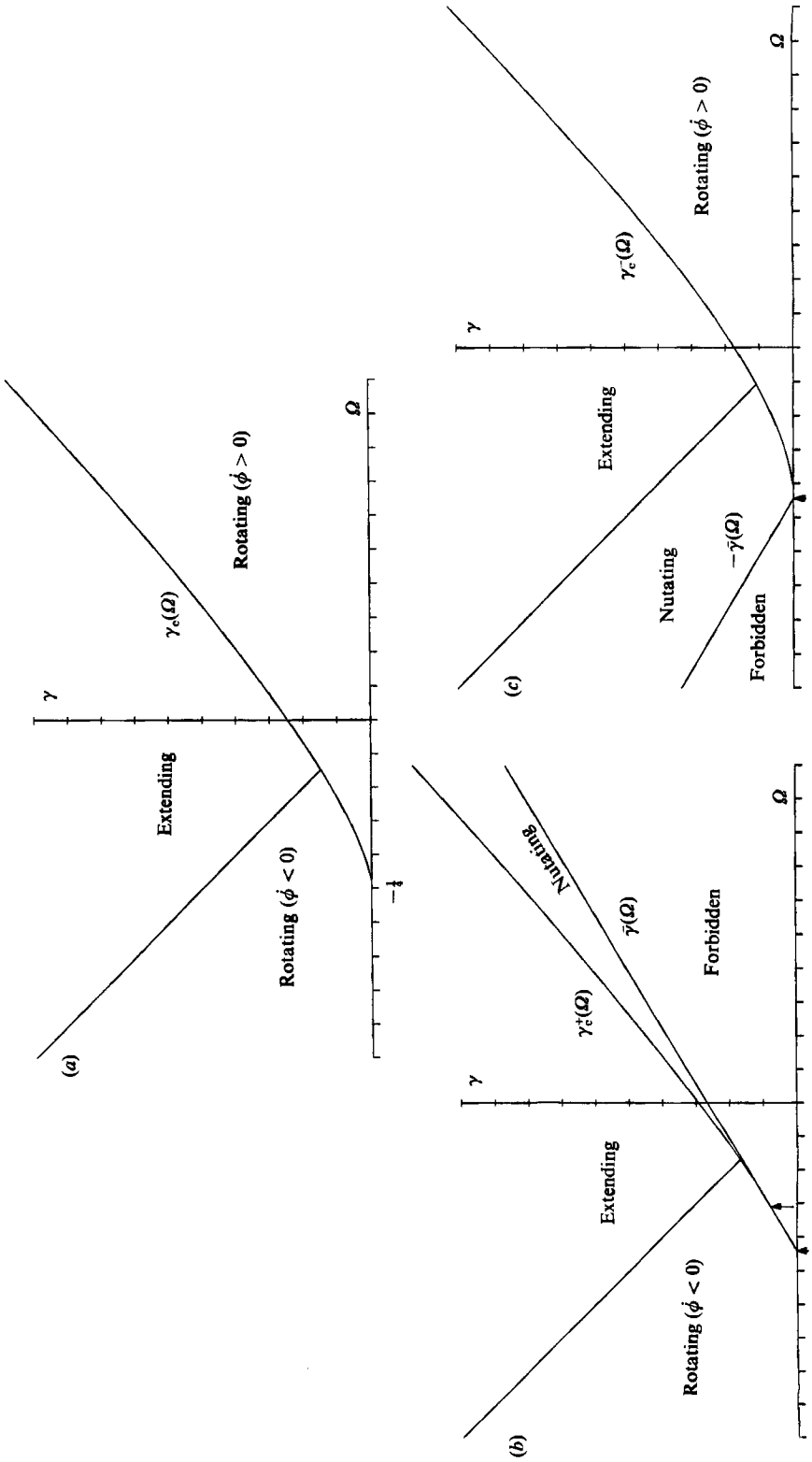

FIGURE 2. The solution domains for (*a*) $\lambda_0 = 1$; (*b*) $\lambda_0 = 2, s = +1$; and (*c*) $\lambda_0 = 2, s = -1$. The strain γ ranges from 0 to $\frac{1}{2}$ along the vertical axis, and the rotation rate Ω ranges from $-\frac{1}{2}$ to $\frac{1}{2}$ along the horizontal axis. The tick marks are spaced at intervals of 0.05 along either axis. The same axes configuration and scaling are used in all subsequent figures, unless otherwise noted. The annotation of axes is therefore omitted.

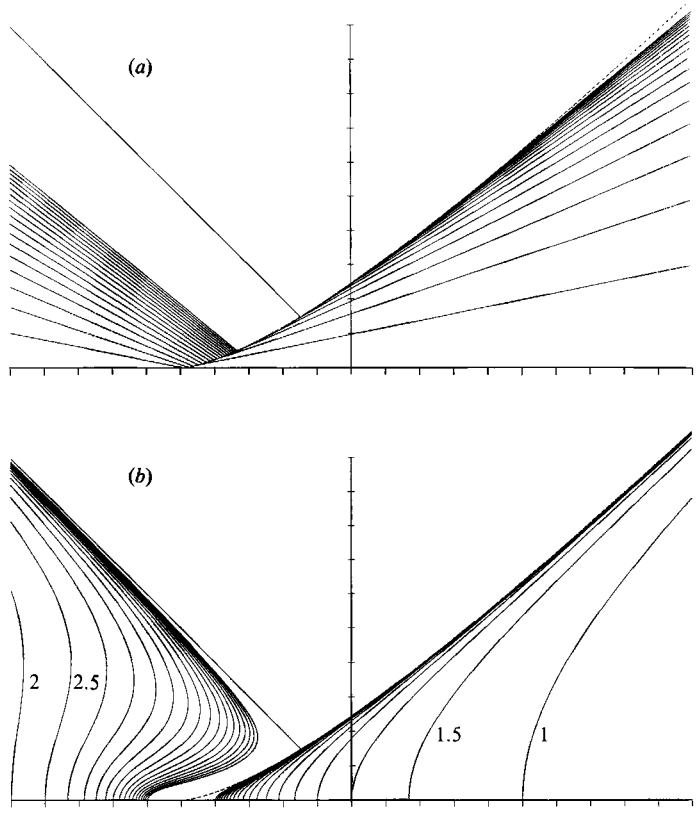

FIGURE 3. Contour maps of (*a*) $\lambda_{\max}$ and (*b*) $T/2\pi$ for $\lambda_0 = 1$. The contour interval is 0.5 in both maps. $\lambda_{\max} = \lambda_0 = 1$ along $\gamma = 0$. A few selected contours of constant $T/2\pi$ are labelled for clarity, and contours for large values of $\lambda_{\max}$ and $T/2\pi$ are omitted.

opposite that for $s = +1$. Otherwise, the domain of solutions is similar to that for $\lambda_0 = 1$.

Finally, as $\lambda_0 \to \infty$, the regions of nutating solutions collapse onto the lines $\gamma = s\Omega$, and the curves $\gamma_c^s(\Omega)$ converge to the lines $\gamma = -s\Omega$.

Two basic properties of the periodic solutions are examined next. Equations (6)–(8) were solved numerically using a standard fourth-order Runge–Kutta integration scheme (with time step $\Delta t = 0.025$) coupled with a Newton–Raphson root-finding technique in order to find the period of evolution, T, and the maximum aspect ratio achieved, $\lambda_{\max}$, for the periodic solutions. (Tests with finer temporal resolution indicate that the results obtained are accurate to within one part in 10^8.) Figure 3 shows maps of $\lambda_{\max}$ and $T/2\pi$ in the (γ, Ω)-plane for $\lambda_0 = 1$. The contours of constant $\lambda_{\max}$ are straight because (3) is linear in γ and Ω. The map of $T/2\pi$ confirms that solutions near the various regional boundaries have large periods. When $\lambda_0 > 1$, there are two sets of maps, one corresponding to each sign s, and in the following pages, three values receive special attention: $\lambda_0 = 2, 3$, and ∞ (a vortex layer). Figure 4 for $\lambda_0 = 2$, $s = \pm 1$ and figure 5 for $\lambda_0 = 3$, $s = \pm 1$ illustrate the variation of $\lambda_{\max}$ and $T/2\pi$ with λ_0 and s. Apart from the domain size, these maps differ little from the map for $\lambda_0 = 1$. For $\lambda_0 \to \infty$, or for an infinitely long vortex layer, almost all of the solutions are rotating, and for these, $\lambda_{\max}/\lambda_0 = (|\Omega| + \gamma)/(|\Omega| - \gamma)$, and $T = \pi/(\Omega^2 - \gamma^2)^{\frac{1}{2}}$ independent of s. The remaining solutions, confined to the lines $\gamma = s\Omega$, are stationary.

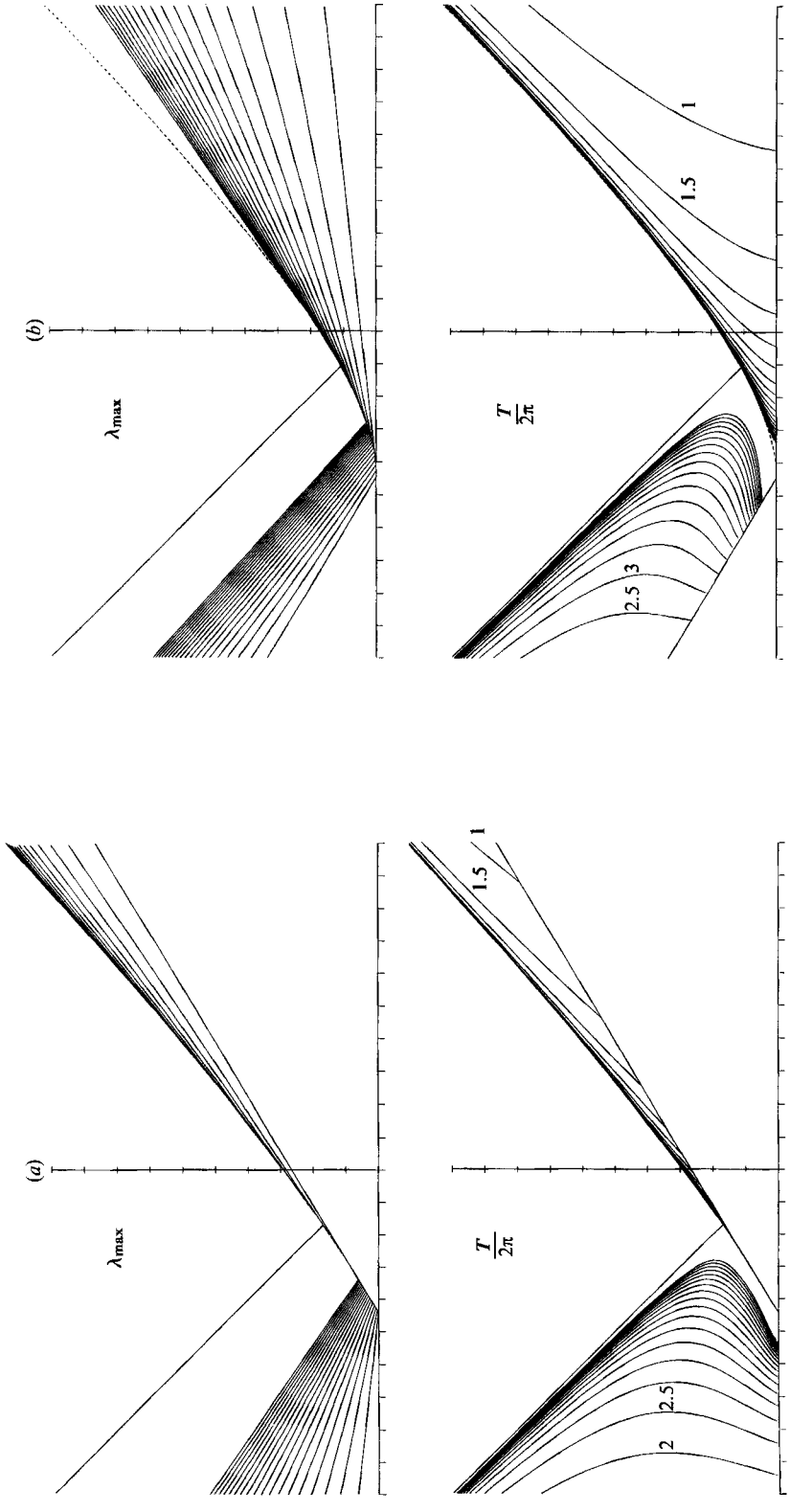

FIGURE 4. Contour maps of λ_{max} and $T/2\pi$ for $\lambda_0 = 2$; and (*a*) $s = +1$, (*b*) $s = -1$. $\lambda_{max} = \lambda_0 = 2$ along $\gamma = 0$ and (*a*) $\bar{\gamma}(\Omega)$, (*b*) $-\bar{\gamma}(\Omega)$. The contour intervals in these maps and subsequent ones are the same as used in figure 3.

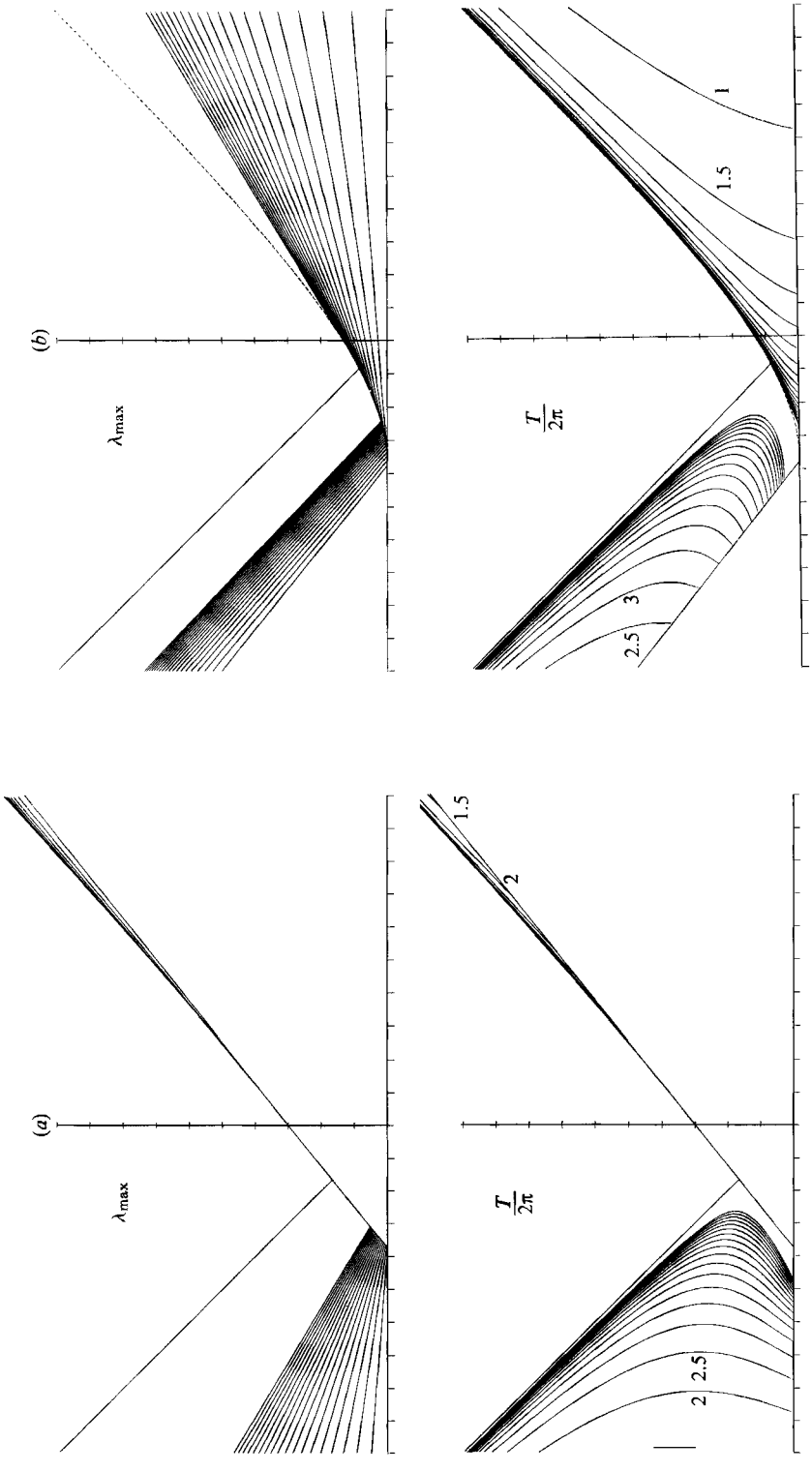

FIGURE 5. Contour maps of λ_{max} (top) and $T/2\pi$ for $\lambda_0 = 3$; and (*a*) $s = +1$, (*b*) $s = -1$.

3. Linear stability

In this section, equations are derived which describe the linear evolution of small boundary disturbances to the time-periodic basic elliptical vortex and, from these equations, growth rates corresponding to eigenmode disturbances are calculated by Floquet theory over an extensive region of parameter space. A result which leads to an enormous simplification of the stability problem is that the eigenmodes for the unstrained elliptical vortex (Love 1893) are precisely the same for the strained one (see below). This allows one to obtain two coupled linear equations (with periodic coefficients) for each mode symmetry, $m\,(m = 3, 4, \ldots)$. A brief sketch of the derivation follows next.

It is convenient to move into a coordinate system x', y' rotating with the undisturbed ellipse, at the rate $\dot{\phi}$ given in (2*b*) (see figure 1). To obtain the velocity of a point in this transformed coordinate system, first note that a point (x, y) in the original coordinate system moves according to

$$\dot{x} = u = u_e + \gamma x - \Omega y, \quad \dot{y} = v = v_e - \gamma y + \Omega x, \tag{12a, b}$$

where

$$\boldsymbol{u}_e = -\frac{1}{2\pi}\oint_{\mathscr{C}} \log|\boldsymbol{x} - \boldsymbol{\xi}|\, d\boldsymbol{\xi} \tag{13}$$

is the velocity due to the vortex alone (including the disturbance). Here, $\boldsymbol{\xi}$ is a point on the contour $\mathscr{C}$ traversed so as to leave the interior of the vortex on the left. So, by taking the time derivative of

$$x' = x\cos\phi + y\sin\phi, \quad y' = y\cos\phi - x\sin\phi, \tag{14}$$

one finds

$$\dot{x}' = u' = u'_e + \gamma(x'\cos 2\phi - y'\sin 2\phi) + (\dot{\phi} - \Omega)\, y', \tag{15a}$$

$$\dot{y}' = v' = v'_e - \gamma(y'\cos 2\phi + x'\sin 2\phi) - (\dot{\phi} - \Omega)\, x', \tag{15b}$$

where $\boldsymbol{u}'_e$ satisfies (13) with $\boldsymbol{x}'$ replacing $\boldsymbol{x}$.

Next, a second coordinate transformation is made, now into elliptical coordinates R and θ, in terms of which

$$x' = (cR + dR^{-1})\cos\theta, \quad y' = (cR - dR^{-1})\sin\theta, \tag{16}$$

with $c = \frac{1}{2}(a+b)$ and $d = \frac{1}{2}(a-b)$. Recall, from figure 1, that a is the length of the semi-major axis, and b is the length of the semi-minor axis ($a = \lambda^{\frac{1}{2}}$ and $b = \lambda^{-\frac{1}{2}}$). $R = 1$ gives the position of the undisturbed vortex boundary.

Now suppose that the disturbed boundary departs only slightly from $R = 1$, and define $\rho(\theta, t) = R(\theta, t) - 1 \ll 1$. Substituting $R = 1 + \rho$ into (16) and discarding terms of $O(\rho^2)$ or higher, one may show

$$\rho = \frac{\eta}{a^2\sin^2\theta + b^2\cos^2\theta}, \tag{17}$$

where

$$2\eta = \frac{x'^2}{a^2} + \frac{y'^2}{b^2} - 1. \tag{18}$$

Working in terms of η proves simplest in what follows. At any particular value of θ, η must satisfy

$$\frac{\partial\eta}{\partial t} + \bar{\Omega}\frac{\partial\eta}{\partial\theta} = \dot{\eta}. \tag{19}$$

Here, $\bar{\Omega}(t) = \dot{\theta}$ is the rate of change of θ following a fluid particle along the *undisturbed* elliptical boundary. Denoting all undisturbed quantities by an overbar,

$$\left.\begin{aligned}\bar{\Omega} &= \frac{\mathrm{d}}{\mathrm{d}t}\tan^{-1}\left(\lambda\frac{\bar{y}'}{\bar{x}'}\right)\\ &= \Omega_{\mathrm{e}} + \frac{2\gamma\lambda\sin 2\phi}{\lambda^2-1}\end{aligned}\right\} \tag{20}$$

(use has been made of (2), (15) and the expressions $\bar{u}'_{\mathrm{e}} = -1/(a+b)\sin\theta$ and $\bar{v}'_{\mathrm{e}} = 1/(a+b)\cos\theta$). The last remaining hurdle is the evaluation of $\dot{\eta}$ in (19). From a time-derivative of (18), and $ab = 1$,

$$\dot{\eta} = b^2 x' u'_{\mathrm{e}} + a^2 y' v'_{\mathrm{e}} - \Omega_{\mathrm{e}}(a^2-b^2)\,x'y', \tag{21}$$

all terms involving ϕ having cancelled exactly. Apart from the implicit time-dependence of a, b, and Ω_{e}, this equation is identical to that obtained in the stability analysis of a freely rotating, unstrained vortex (Love 1893). Therefore, since $\bar{\Omega}$ in (19) does not depend on θ, both the strained and unstrained linear problems have identical θ-structure; that is to say,

$$\eta(\theta, t) = \mathrm{Re}\,[A(t)\cos m\theta + B(t)\sin m\theta] \tag{22}$$

is the eigenmode in both cases. Finally, then, carrying Love's results over to the strained problem,

$$\dot{A} = -\left[m\bar{\Omega} - \frac{1}{2} + \frac{1}{2}\left(\frac{\lambda-1}{\lambda+1}\right)^m\right]B, \tag{23a}$$

$$\dot{B} = +\left[m\bar{\Omega} - \frac{1}{2} - \frac{1}{2}\left(\frac{\lambda-1}{\lambda+1}\right)^m\right]A. \tag{23b}$$

It is noteworthy that these equations hold for any γ and Ω, not just those values that permit periodic solutions. Indeed, γ and Ω need not even be steady.

For the periodic Kida solutions, the coefficients in the disturbance equations (23) generally vary periodically with time, and so one can assess linear stability by Floquet theory (Abramowitz & Stegun 1965, p. 727). In Floquet theory, the amplification of the disturbance over a full period matters, and the eigenfunctions are those choices of A and B which amplify (or decay) by the same amount each period. The eigenfunctions and corresponding amplification factors, or eigenvalues, are determined by solving (23) with two independent initial conditions, say

$$\left.\begin{aligned}A_1(0) = 1, \quad B_1(0) = 0,\\ A_2(0) = 0, \quad B_2(0) = 1,\end{aligned}\right\} \tag{24}$$

and seeking constants c_1, c_2, and μ such that the eigenfunction

$$A(t) = c_1 A_1(t) + c_2 A_2(t), \quad B(t) = c_1 B_1(t) + c_2 B_2(t) \tag{25}$$

satisfies after one period, $t = T$,

$$A(T) = \mu A(0), \quad B(T) = \mu B(0). \tag{26}$$

Using (24), one obtains two algebraic equations

$$(A_1(T)-\mu)\,c_1 + A_2(T)\,c_2 = 0, \quad B_1(T)\,c_1 + (B_2(T)-\mu)\,c_2 = 0 \tag{27}$$

whose solvability requires

$$\mu = \tfrac{1}{2}(A_1(T)+B_2(T)) \pm \tfrac{1}{2}[(A_1(T)-B_2(T))^2+4A_2(T)\,B_1(T)]^{\frac{1}{2}}. \tag{28}$$

This is the amplification through one full period. The average rate of amplification through one period is therefore

$$\sigma = T^{-1}\,\mathrm{Re}\,[\log \mu], \tag{29}$$

and the 'growth rate' is defined to be the largest of the two σ values (corresponding to the two values of μ in (28)).

The quantities $A_1(T)$ etc. were obtained by integrating the disturbance equations (23) simultaneously with the basic-state equations (6)–(8) through one period. As described earlier, the period T is known to 1 part in 10^8 via separate integration of the basic-state equations. The time step is chosen to be about 0.025, in such a way that an integral number of time steps comprise one period. Tests with finer temporal resolution indicate that, at worst, the growth rate is accurate to six decimal places.

Maps of $\sigma(\Omega, \gamma; m; \lambda_0, s)$ are presented next corresponding to the parameter values λ_0 and s used in figures 3–7 (recall that λ_0 is the minimum aspect ratio and $s = \sin 2\phi$ when $\lambda = \lambda_0$). The disturbance wavenumber m ranges from 3 to 8 with maps shown for 3, 4, 5, and 3–8 inclusive (the wavenumbers $m = 0$, 1, and 2 can be excluded because they do not alter the elliptical form of the basic solution). Figure 6, for $\lambda_0 = 1$, reveals a complex network of instability patches or lobes, predominantly in the left region. Instability in the right region appears concentrated near the curve $\gamma_c(\Omega)$ (dashed line) apart from a few downward bulges. It is important to emphasize that the $\sigma = 0$ contour is not displayed but, if it were, one would see that all of the lobes in the left-hand region actually interconnect like a patchwork quilt (see, for example, figure 7). In the regions between the lobes, the growth rate is precisely zero (both roots of (28) give $\sigma = 0$ from (29)), implying *neutral* stability (disturbances neither grow nor decay, according to linear theory). Remarkably, the quilted structure of the growth rate extends across the line of zero strain, where lobes connect with their images at an infinite number of points $\Omega = \Omega_{mn}$, $n = 0, \pm 1, \pm 2, \ldots$ given by

$$\Omega_{mn} = -\frac{1}{4}\frac{2n+4-3m}{2n-m} \tag{30}$$

(see figure 8). That is, *arbitrarily small strain rates can destabilize the vortex*. The source of the instability is the resonance of the disturbance frequency with a harmonic of the basic-state rotational frequency $\dot{\phi}$ (both frequencies tending to constant values as $\gamma \to 0$). The same kind of behaviour occurs for the Mathieu equation, see Abramowitz & Stegun (1965, pp. 721–730). Ω_{mn} accumulates onto the value $\Omega = -\frac{1}{4}$ from both sides as $|n| \to \infty$, explaining the increasingly complex pattern of instability lobes as Ω approaches $-\frac{1}{4}$. Remarkably, one can find an m and an n corresponding to any rational value of Ω, implying that all rational values of Ω are resonantly unstable as $\gamma \to 0$ (and all irrational values are stable!). While this is an interesting mathematical result, it should be emphasized that the growth rates are very small, diminishing as γ^m.

Consider next the results for $\lambda_0 = 2$ (figures 9 and 10). The maps for both signs s have the same qualitative features seen in the case for $\lambda_0 = 1$, namely the quilted network of instability lobes in the left region and the comparatively stable right region. Resonances again arise from the correspondence of the disturbance frequency ν_m (defined below) with a harmonic of the basic-state rotational frequency that lead

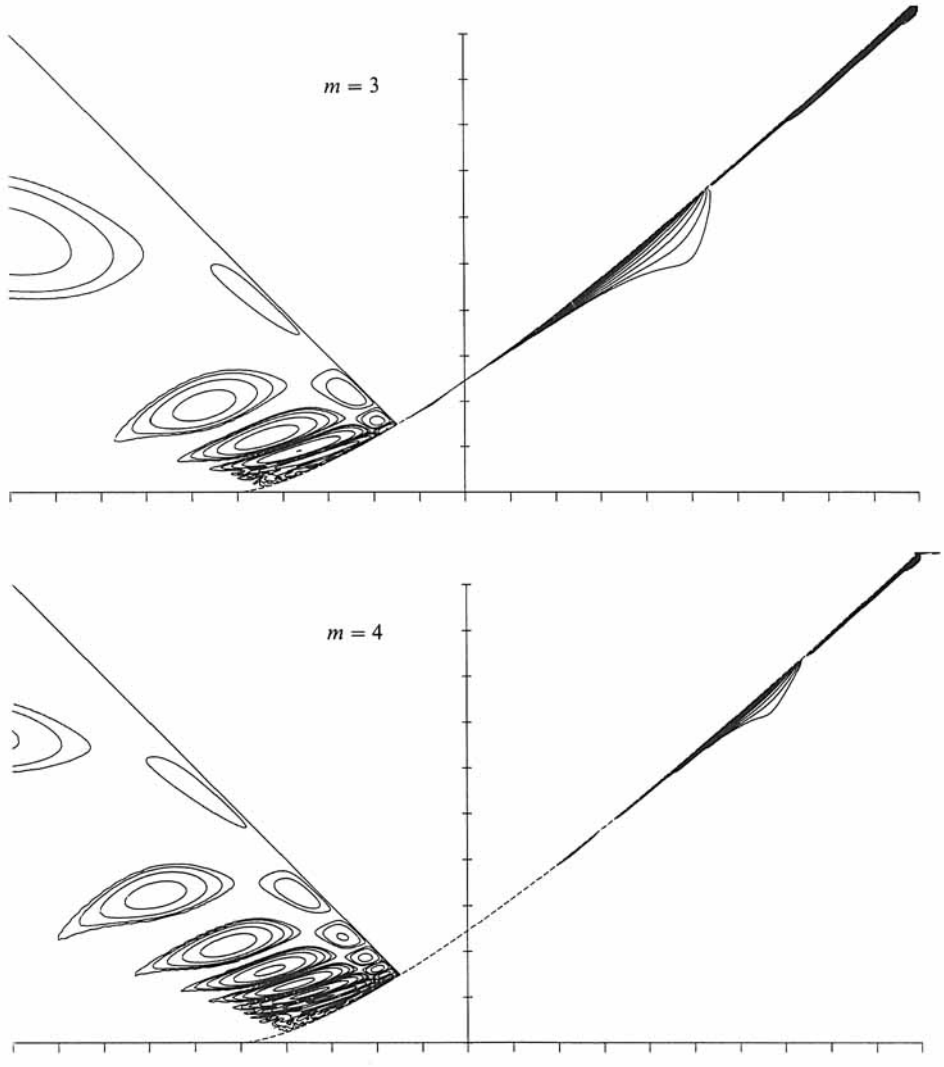

FIGURE 6. For caption see facing page.

to (weak) instability at arbitrarily small γ. The resonances stem from the Ω-axis at the points $\Omega = \Omega_{mn}(\lambda_0)$, $n = 1, 2, \ldots$, with

$$\Omega_{mn} = \Omega_0 - \frac{s\nu_m}{n} \tag{31}$$

and

$$\nu_m = \left[(m\Omega_0 + \tfrac{1}{2})^2 - \frac{1}{4}\left(\frac{\lambda_0 - 1}{\lambda_0 + 1}\right)^{2m}\right]^{\frac{1}{2}}.$$

$\pm\nu_m$ are the frequencies of modes on an elliptical contour of aspect ratio λ_0 in the absence of strain. The ν_m are real quantities for all m as long as $\lambda_0 \leqslant 3$, but, for $\lambda_0 > 3$, ν_3 becomes imaginary followed in turn by ν_4, ν_5, etc. for larger values of λ_0 (Love 1893; see below). Resonances also occur along the lower boundary of the region of nutating solutions (the right region for $s = +1$ and the left one for $s = -1$). Here, the disturbance frequency resonates with harmonics of the basic-state nutational frequency (details omitted).

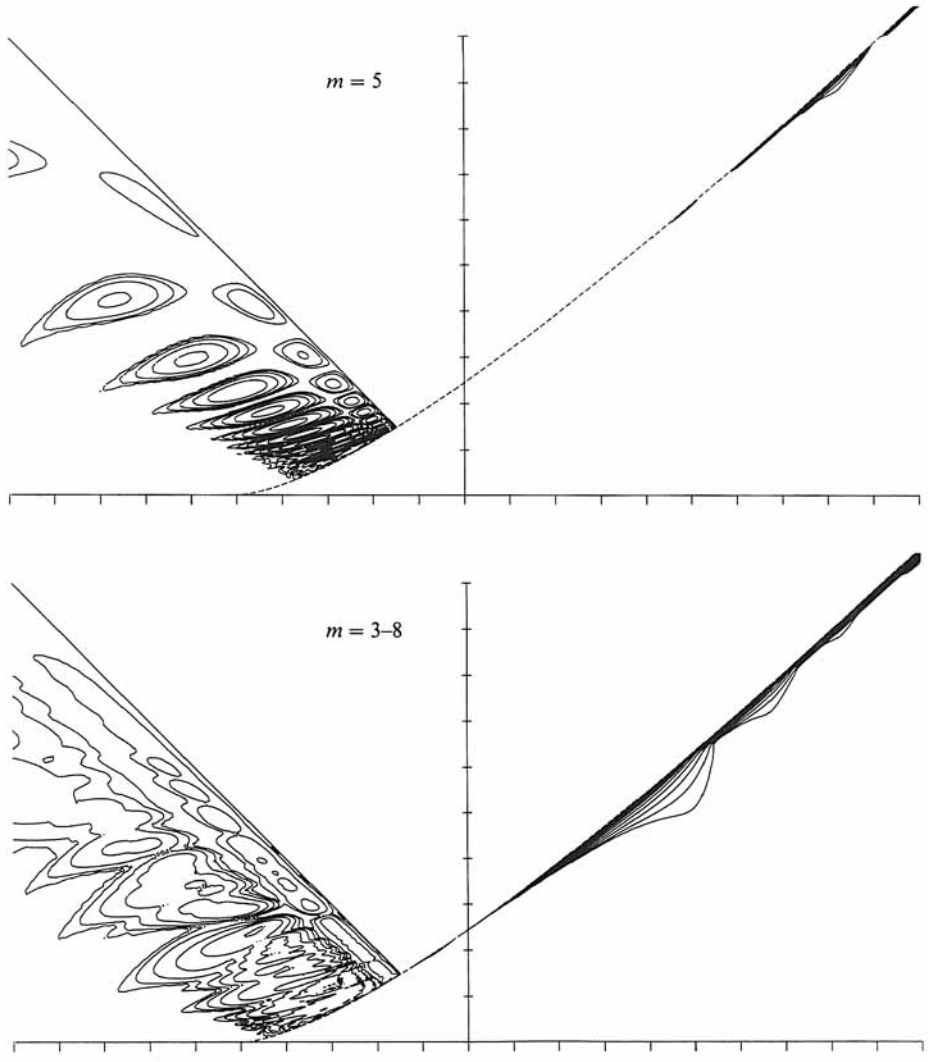

FIGURE 6. Contour maps of growth rate σ when $\lambda_0 = 1$ for various values of the disturbance wavenumber m as labelled on the figure. The contour interval is 0.01, and the lowest level contoured is $\sigma = 0.01$. The small-scale waviness of the lowest contour levels is produced by the contouring routine and is not reflective of inaccuracies in the computed growth rate. The inclusion of higher wavenumbers ($m > 8$) significantly alters the final, summary diagram only in the vicinity of the line $\gamma = -\Omega$, where the basic solutions achieve a large maximum aspect ratio during their periodic evolution thereby enabling the various terms within the brackets of (23) to have comparable magnitude.

The results for $\lambda_0 = 3$ are displayed in figures 11 and 12. Except for $m = 3$, the growth-rate patterns qualitatively parallel those for $\lambda_0 = 2$. In the maps for $m = 3$, one lobe of instability now covers a substantial part of the regions of rotating solutions (the left region for $s = +1$ and the right one for $s = -1$) and extends down to $\gamma = 0$ where the growth rate must vanish ($\nu_3 = 0$). A further increase in λ_0 renders the solutions along $\gamma = 0$ unstable first to $m = 3$ and then to higher-m disturbances in turn. That is, the maps for $m = 4, 5$, etc. go through the same sequence of morphological changes seen for $m = 3$ at larger and larger values of λ_0.

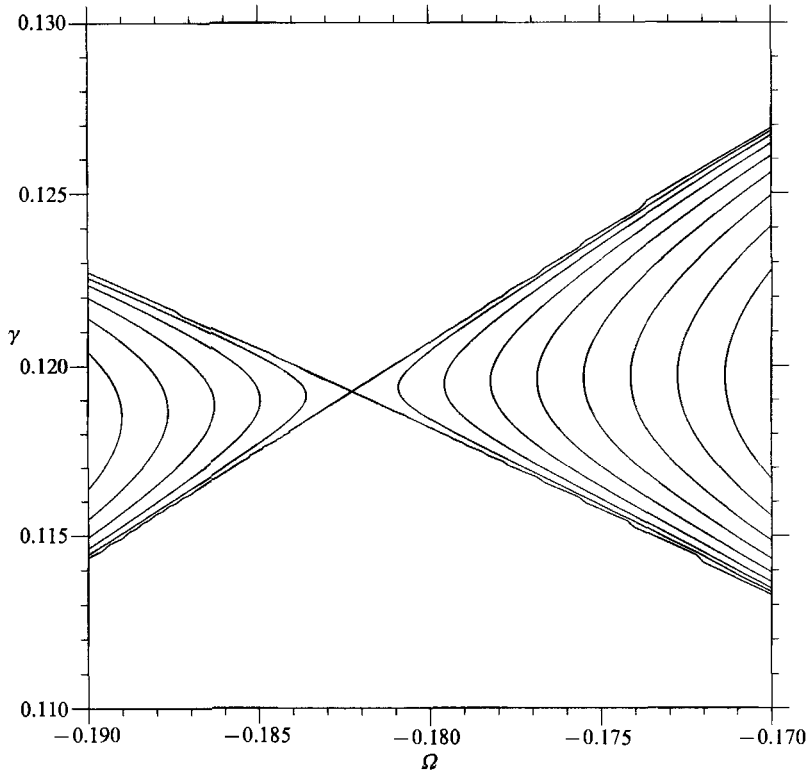

FIGURE 7. A close-up view of the $m = 3$ stability diagram in figure 6 in the range $-0.19 \leqslant \Omega \leqslant -0.17$, $0.11 \leqslant \gamma \leqslant 0.13$ (recall that the tick marks on the axes in figure 6 are separated by 0.05). The minimum contour level plotted is $\sigma = 1 \times 10^{-8}$, and the contour interval is 1×10^{-3}. (In this range of γ and Ω, the computed growth rate is accurate to 12 decimal places.)

As $\lambda_0 \to \infty$, the problem becomes one of assessing the stability of an infinite vortex layer in the presence of a rotating strain field. In this limit, it is appropriate to set $m = \frac{1}{2}k\lambda_0$ with k infinite, for then one recovers Rayleigh's (1894) dispersion relation for disturbances to an unstrained vortex layer; namely $\nu^2(k) = \frac{1}{4}[(k-1)^2 - e^{-2k}]$ (see (34) below). k is therefore to be identified as the product of a dimensional wavenumber and the width of the layer. Rayleigh showed that the range of wavenumbers $0 < k < 1.27846454\ldots$ is unstable and maximally so at $k = 0.79681213\ldots$ at which value $\operatorname{Im}\nu = 0.20118558\ldots$.

When $\gamma > 0$, the layer rotates while periodically thinning and thickening (except in a few special cases noted below), and one can again turn to Floquet theory to assess stability. Taking the limit $\lambda_0 \to \infty$ in (3) provides us with a direct relationship between the relative layer thickness Δ, or $\lambda_0/\lambda(t)$, and the orientation angle ϕ, namely

$$\Delta = \frac{\Omega - \gamma \sin 2\phi}{\Omega - \gamma s}, \tag{32}$$

whereas (2b) for $\dot{\phi}$ simplies to

$$\dot{\phi} = \Omega - \gamma \sin 2\phi. \tag{33}$$

The actual thickness of the layer does not matter, because neither the original equations of motion nor the fluid domain depend on a lengthscale. Now, in order to

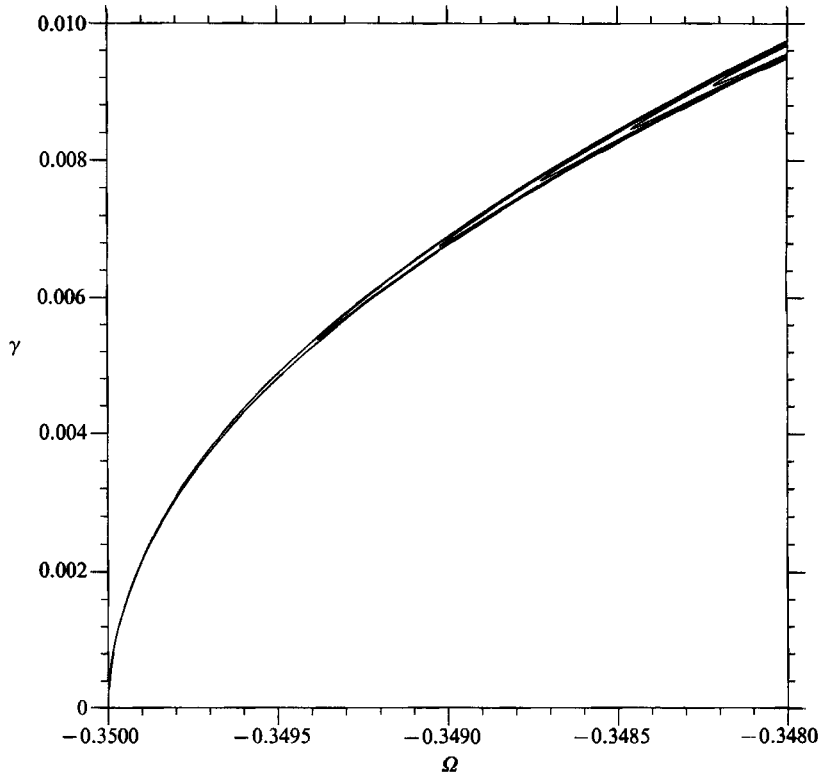

FIGURE 8. A close-up view of the $m = 3$ stability diagram in figure 8 near the $\Omega = \Omega_{3,-1}$ resonance, $-0.35 \leqslant \Omega \leqslant 0.348$ and $0 \leqslant \gamma \leqslant 0.01$ (note the distorted scale). The minimum contour level is $\sigma = 1 \times 10^{-9}$, and the contour interval is 2×10^{-5}. A careful inspection reveals that the ridge of peak instability follows the curve $\gamma \approx 0.215(\Omega - \Omega_{3,-1})^{\frac{1}{2}}$, that the Ω-width of the instability band scales as γ^4, and that the growth rate along the ridge of instability is $\sigma \approx 129\gamma^3$. Similar behaviour has been found for all other resonant-Ω values inspected, specifically $\Omega_{3,0} = -\frac{5}{12}$, $\Omega_{3,1} = \frac{1}{4}$, and $\Omega_{3,-2} = -\frac{9}{28}$.

obtain disturbance equations for the layer, it is again appropriate to set $m = \frac{1}{2}k\lambda_0$ with k finite, and in the limit $\lambda_0 \to \infty$, (23) becomes

$$\dot{A} = -\tfrac{1}{2}[k\Delta(1 + 2\gamma \sin 2\phi) - 1 + \mathrm{e}^{-k\Delta}]B, \tag{34a}$$

$$\dot{B} = +\tfrac{1}{2}[k\Delta(1 + 2\gamma \sin 2\phi) - 1 - \mathrm{e}^{-k\Delta}]A. \tag{34b}$$

These equations extend those derived by Rayleigh to rotating, extending and compressing layers.

As above, two independent solutions of these equations are calculated by numerical integration, and the results after one period are used to calculate the growth rate. The new feature here is that the disturbance wavenumber k ranges over a continuum of values, $k > 0$.

Figure 13 gives maps of the growth rate corresponding to $k = 0.79681213$, 1.27846454, 2, and 0–5 inclusive, with the results for $s = +1$ plotted in the left region and those for $s = -1$ in the right region. These maps show the dramatic transition that takes place upon crossing the margin of stability for the unstrained layer. The case $k = 2$ shows an infinite sequence of resonant instabilities along $\gamma = 0$; these occur at the values $\Omega_n(k) = \pm\nu(k)/n$, $n = 1, 2, \ldots$, and accumulate on the origin. This

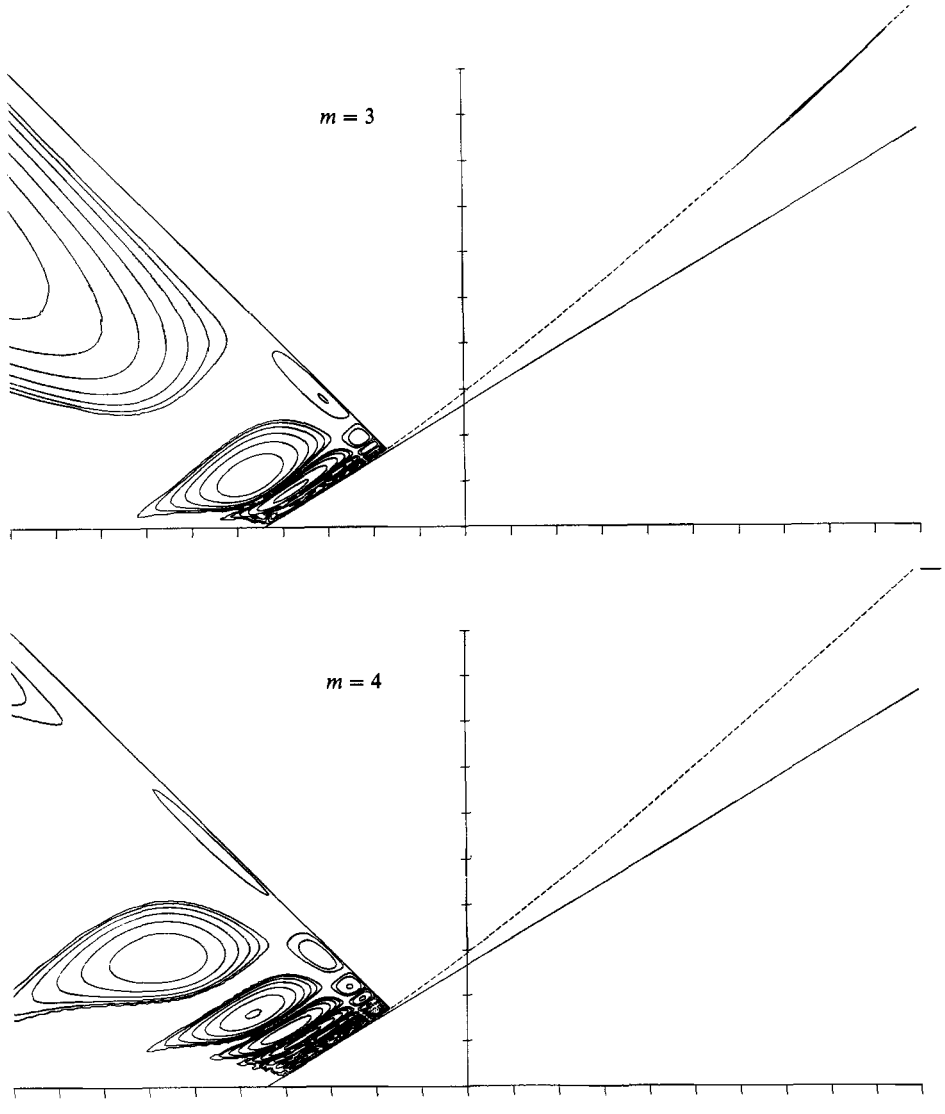

FIGURE 9. For caption see facing page.

map is analogous to the maps above for $\lambda_0 < 3$. The map for $k = 1.27846454$ is on the transition of instability for the unstrained solutions, like the $m = 3$ maps for $\lambda_0 = 3$. In the map for $k = 0.79681213$, the principal lobes of instability centre themselves on the line $\gamma = 0$.

The map for $k = 0$ to 5 inclusive (maximum growth rate) shows that layers which experience a great degree of thinning during their evolution are less unstable, and significantly so, than an unstrained, unthinned layer. The type of straining flow which most accentuates this thinning has $|\Omega| - \gamma \ll |\Omega| + \gamma$ (see (32)), corresponding to a nearly uniform shear flow.

Excluded from the discussion thus far are the stationary solutions of infinite aspect ratio along the lines $\gamma = s\Omega$, the remnants of the nutating-solution regions for finite λ_0. These stationary solutions correspond to vortex layers in uniform shear, and their stability has also been determined by Rayleigh (1894) (see also Dritschel 1989*a* for

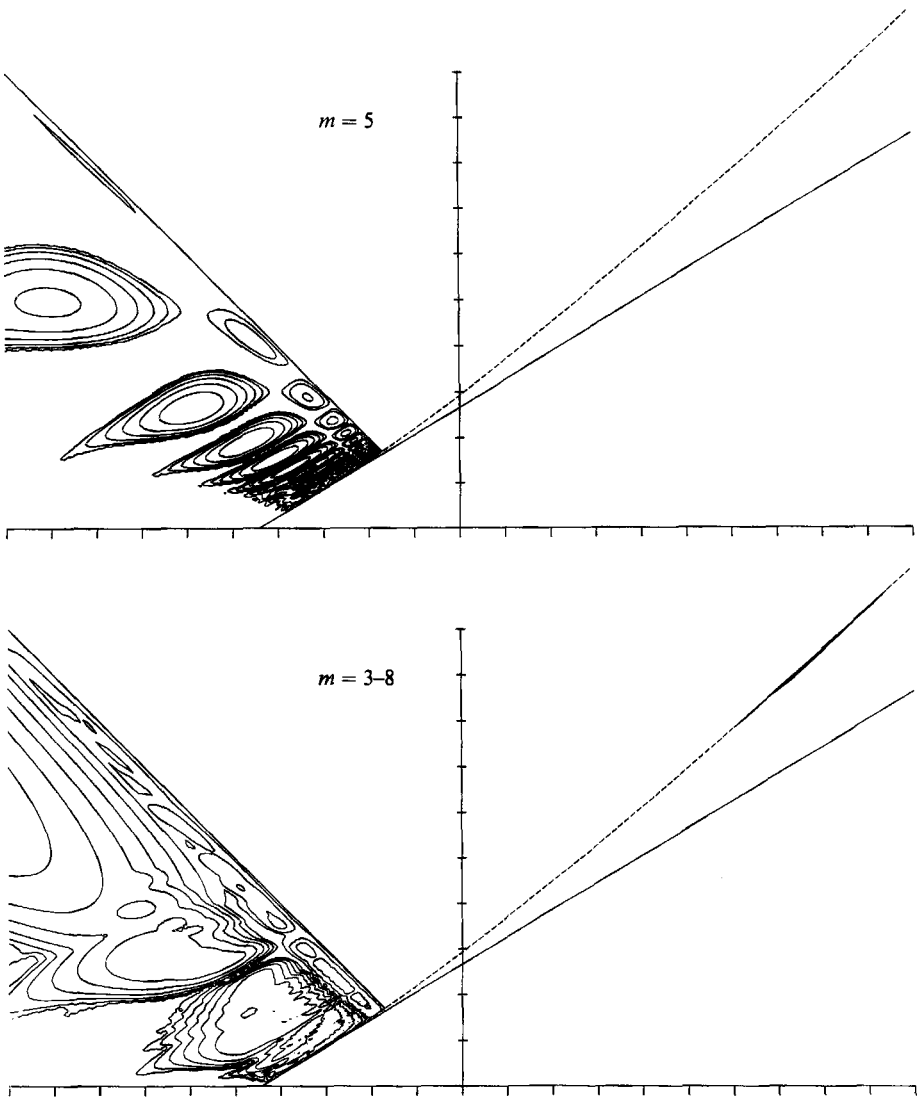

FIGURE 9. Contour maps of growth rate σ when $\lambda_0 = 2, s = +1$. The contour levels in these maps and those to follow are the same as used in figure 6 ($\Delta\sigma = 0.01$ between contours).

further details and remarks on nonlinear stability). Basically, stability follows if the eigenfrequencies $\nu(k)$ satisfy

$$\nu^2(k) = \tfrac{1}{4}[(k(1-2\gamma s)-1)^2 - e^{-2k}] \geqslant 0 \tag{35}$$

for all wavenumbers k (see (34) with $\sin 2\phi = -s$). Here, $A \equiv 2\gamma s$ is just the external shear. For $A \geqslant 1$ then, a vortex layer is completely stable. For the unstable values of A, the peak growth rate is very weak near $A = 1$, only $\frac{1}{2}\exp(1/1-A)$ approximately, and tends monotonically to the constant value of $\frac{1}{2}$ as $A \to -\infty$.

Finally, consider the stability of the stationary solutions of all aspect ratios as a function of λ_0 and Ω (note: results for the special case $\Omega = 0$ were presented by Moore & Saffman 1971). For a given λ_0, the stationary solutions occupy the lines $\gamma = 0$ and $\gamma = s\bar{\gamma} = s[(\lambda_0^2-1)/(\lambda_0^2+1)](\Omega-\Omega_0)$, $s = \pm 1$. Now since the coefficients of the

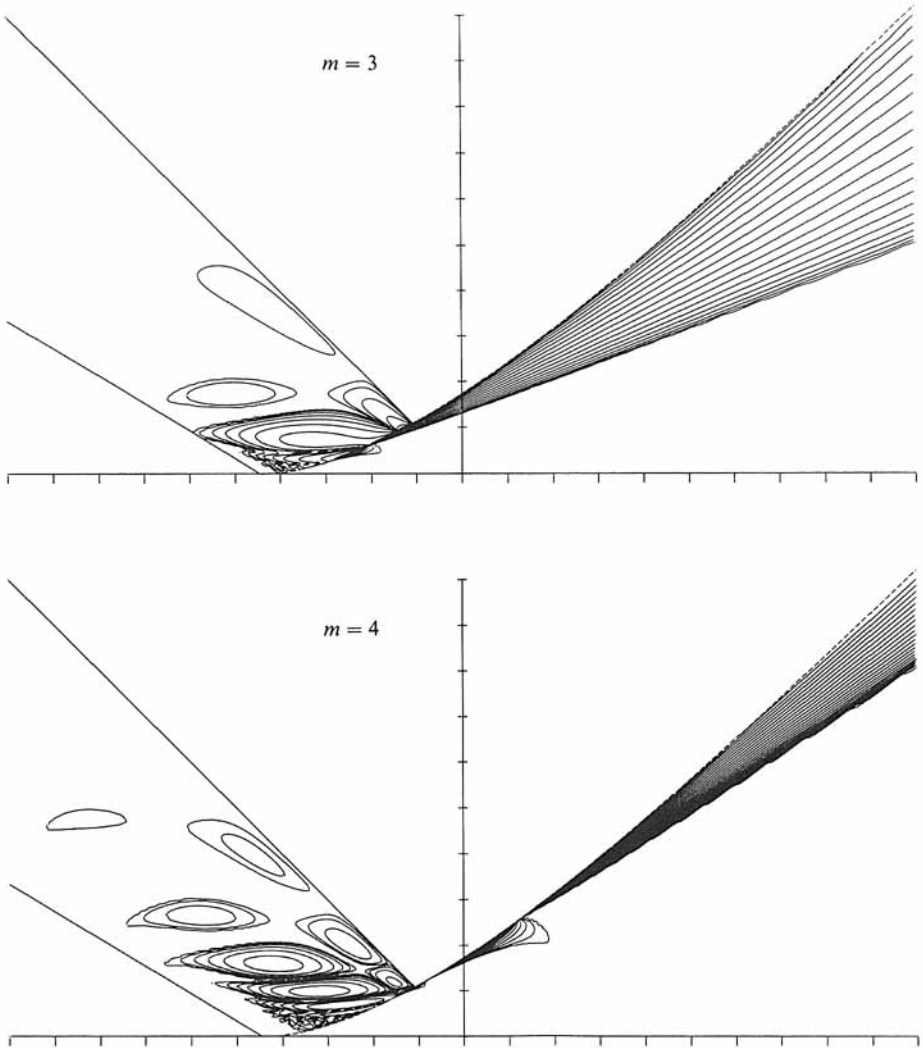

FIGURE 10. For caption see facing page.

stability equations (23) are time-independent, one can immediately write down the dispersion relation for the eigenfrequencies ν_m:

$$\nu_m = \left[(m\bar{\Omega} - \tfrac{1}{2})^2 - \frac{1}{4}\left(\frac{\lambda_0 - 1}{\lambda_0 + 1}\right)^{2m}\right]^{\frac{1}{2}}, \tag{36}$$

where $\bar{\Omega} = (1+2\Omega)\lambda_0/(\lambda_0^2+1)$. The case $\Omega = \Omega_0$ corresponds to $\gamma = 0$, and, in general, $\gamma = |\bar{\gamma}|$ with s equal to the sign of $\bar{\gamma}$. In figure 14, maps are displayed of γs, $\mathrm{Im}\,\nu_3$, $\mathrm{Im}\,\nu_4$, and $\mathrm{Im}\,\nu_5$ as a function of λ_0^{-1} (x-axis) and Ω (y-axis). The growth rates along the curve for $\gamma = 0$ are just those that Love (1893) obtained for the unstrained elliptical vortex. But, curiously, instability extends all the way to $\lambda_0 = 1$ where the strain vanishes, and there the instability terminates at the values $\Omega = -(m-1)/2m$. These values of the rotation rate just arrest the motion of the m-fold symmetric linear waves on an unstrained, circular vortex. So, once again, arbitrarily weak strain can destabilize an arbitrarily circular, basic-state vortex. On another note, the case

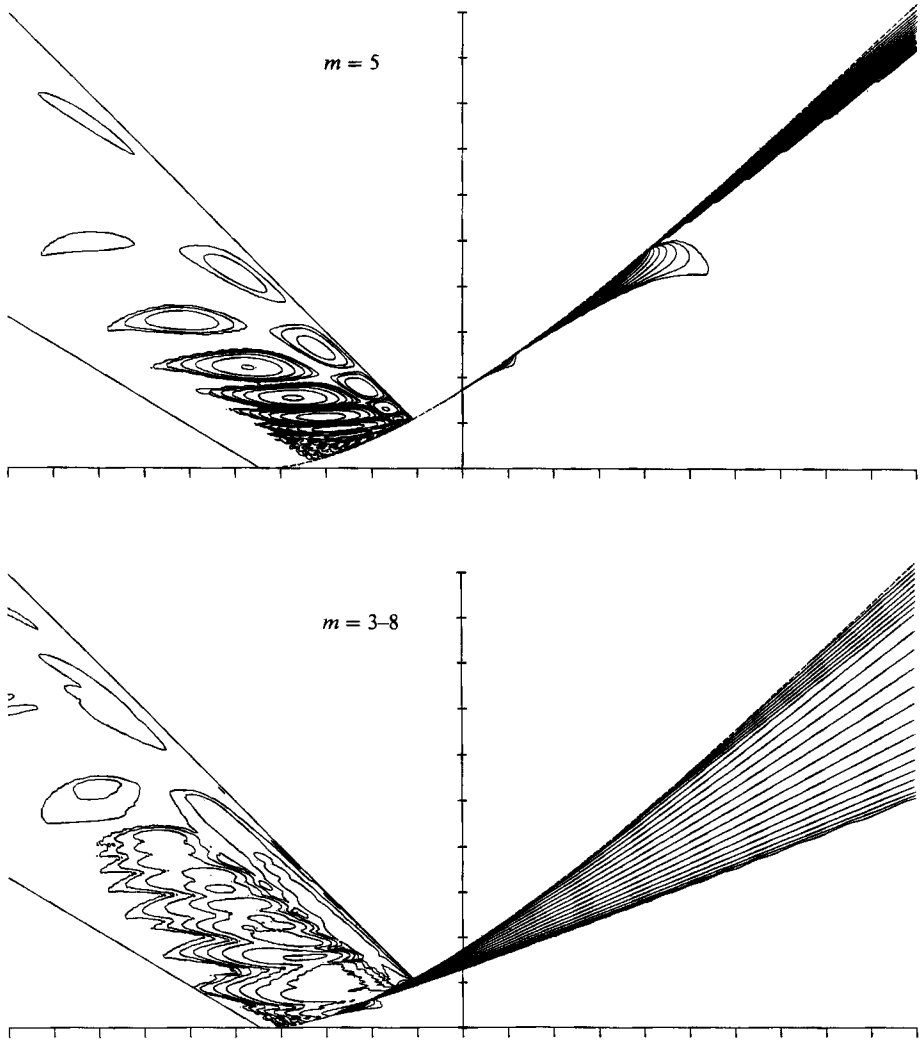

FIGURE 10. Contour maps of growth rate σ when $\lambda_0 = 2, s = -1$.

$m = 2$, previously excluded, here deserves attention. One can show that 'instability' to an $m = 2$ disturbance occurs between $\Omega = \Omega_0$ and

$$\Omega_1 \left(= \Omega_0 + \left(\frac{\lambda_0 - 1}{\lambda_0 + 1}\right)^2 \left(\frac{\lambda_0^2 + 1}{4\lambda_0}\right)\right)$$

– this is just the range of Ω for which $s = +1$ nutating solutions do not exist, see figure 2(*b*). So, the 'instability' is linked with non-existence of periodic solutions in the vicinity of the line of steady solutions between $\Omega = \Omega_0$ and Ω_1.

4. Nonlinearity

The validity of linear theory for the evolution of finite-amplitude disturbances may be questioned on two grounds. First, exponential growth associated with linear

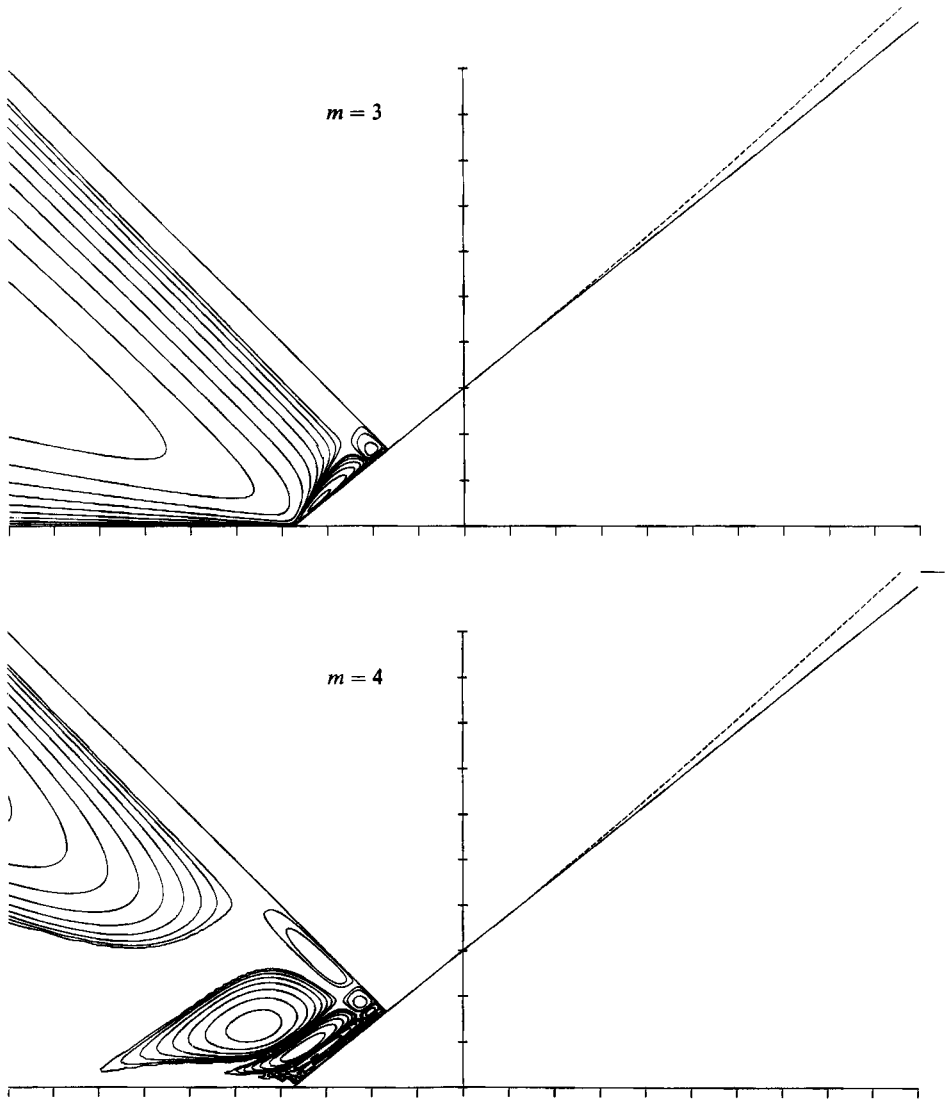

FIGURE 11. For caption see facing page.

instability cannot continue indefinitely, and second, linear stability does not preclude nonlinear instability, even for disturbances of arbitrarily small initial amplitude. This is because linearly stable disturbances are only neutrally stable. An initially 'pure' disturbance, one consisting of a single wavenumber m, interacts with itself and the basic flow to excite other wavenumbers which in turn interact with one another, the initial wavenumber, and the basic flow to generate yet other wavenumbers, and so on. Take, for example, a straining flow with $\gamma = 0.12$ and $\Omega = 0$ and subject an initially circular vortex to either of two boundary disturbances, $\epsilon \cos 3\theta$ or $\epsilon \sin 3\theta$, with ϵ small. The two disturbances correspond to the initial conditions used for the first and second Floquet solutions, (A_1, B_1) and (A_2, B_2), of the previous section. After one period of nonlinear evolution, calculated using a contour-dynamical algorithm (see below) at sufficiently high resolution to free the results of

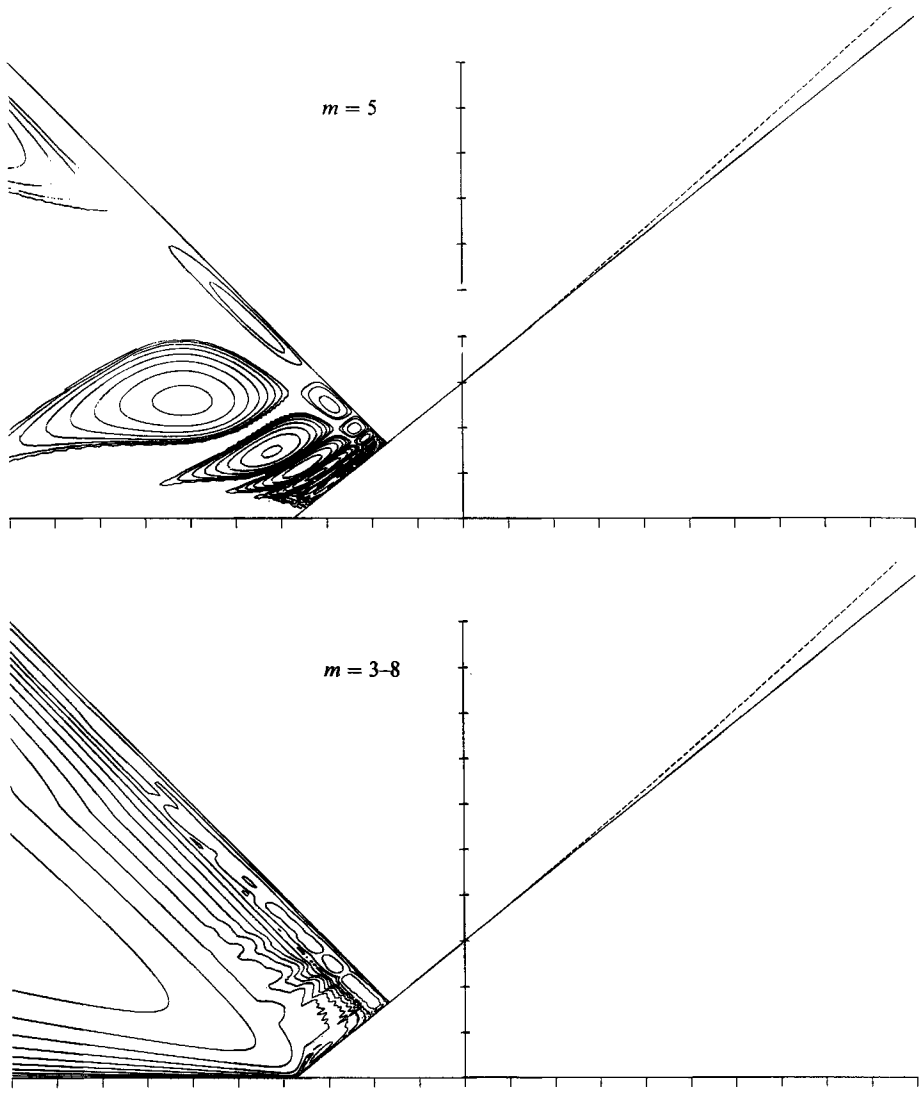

FIGURE 11. Contour maps of growth rate σ when $\lambda_0 = 3, s = +1$.

significant numerical error, the vortex boundary was spectrally analysed (with the same accuracy considerations) and compared to that expected by linear theory. Results for $\epsilon = 0.002$, 0.001, and 0.0005 are listed in table 1. Note that the discrepancies between the nonlinear and linear spectral coefficients scale with ϵ^2 for even m and ϵ^3 for odd m. It is suggested that the quadratic interaction between the original harmonic and itself coupled with the two-fold symmetry of the basic flow generates all the even disturbances at $O(\epsilon^2)$, whereas the nonlinear generation of odd disturbances requires either a cubic interaction between the original wavenumber and itself (and the basic flow) or the interaction between the original wavenumber and an even wavenumber, already of quadratic order, and the basic flow.

Just as in the example just discussed, it is possible to reproduce the linear Floquet results through one period to any desired accuracy using fully nonlinear calculations

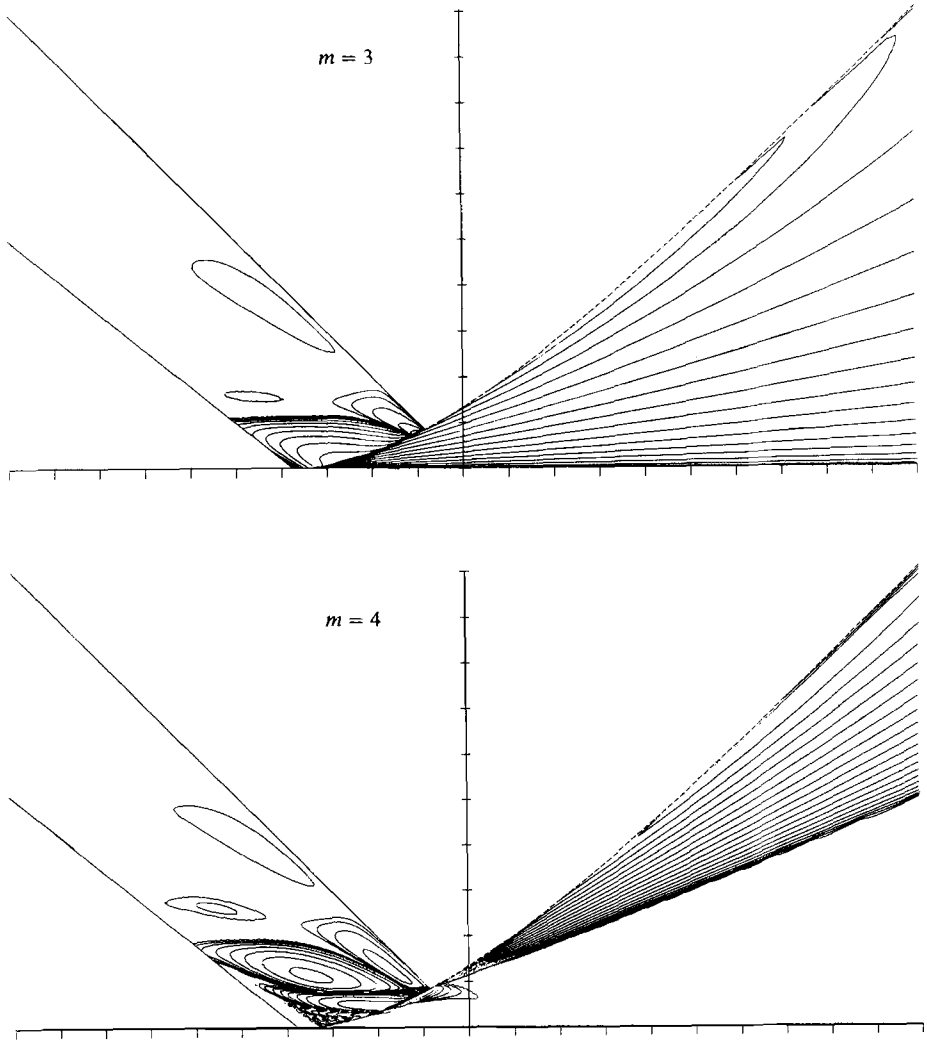

FIGURE 12. For caption see facing page.

for any basic flow and disturbance wavenumber. Even so, the nonlinear calculations and the linear analysis do not always agree on the ultimate stability of a basic flow, and the disagreement is not due to inadequate numerical resolution.

It is perhaps best to briefly discuss the numerical algorithm before proceeding. The algorithm, 'contour surgery' (Dritschel 1988*a*, 1989*b*), fundamentally extends 'contour dynamics' (Zabusky, Hughes & Roberts 1979) by allowing for the automatic removal of fine-scale vorticity features at scales typically four to five orders of magnitude smaller than the scale of the entire vorticity distribution. This approximation enables one to continue contour-dynamical calculations, accurately, well beyond the limits of contour dynamics itself by lessening the computational burden. The algorithm depends on four parameters: L, the scale of the vorticity distribution ($L = 1$ throughout); μ, a parameter proportional to the distance between points on a contour; δ, the smallest scale resolved; and Δt, the time step. In this paper, accuracy is measured in two ways: by the maximum fractional discrepancy

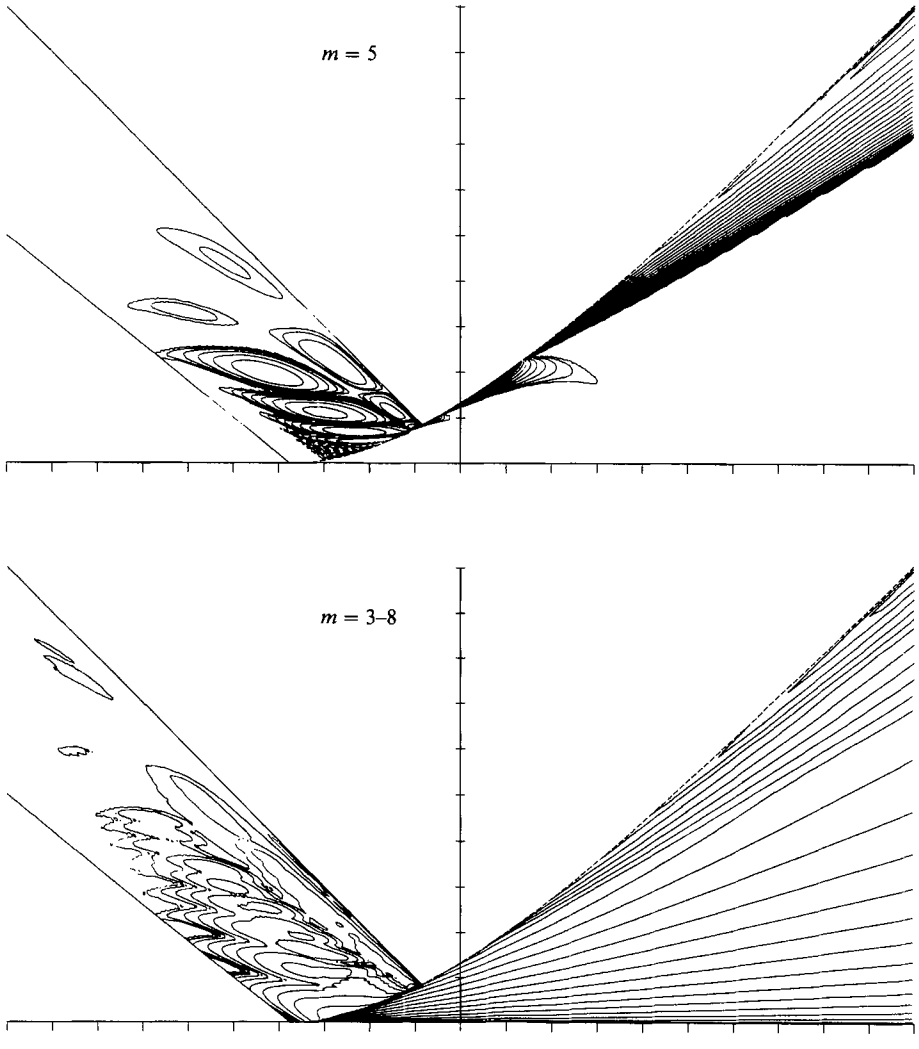

FIGURE 12. Contour maps of growth rate σ when $\lambda_0 = 3, s = -1$.

between the computed area and the initial area of the vortex, ϵ_f (including any bits that get disconnected by surgery); and by the 'phase' error (Dritschel 1989*b*),

$$\epsilon_A(t = n\,\Delta t) = \frac{\omega\,\Delta t}{A(0)} \sum_{k=1}^{n} |A(k\,\Delta t) - A(0)|, \tag{37}$$

where $A(t)$ is the computed area of the vortex at time t, and ω is the jump in vorticity across the vortex's edge ($\omega = 1$).

Reported first are the results of 234 moderate-resolution calculations used to determine the margin of apparent nonlinear stability for strained, initially circular vortices. All of the calculations begin with exactly the same initial conditions and use the same algorithm parameters, $\mu = 0.03$, $\delta = 0.000\,13$, and $\Delta t' \equiv \Delta t/2\pi = 0.05$. Initially, 240 points or nodes resolve the vortex, and each of these nodes is displaced radially by a random number uniformly distributed between -10^{-4} and 10^{-4}. Nonlinear stability is judged by monitoring the variation of the number of nodes: if

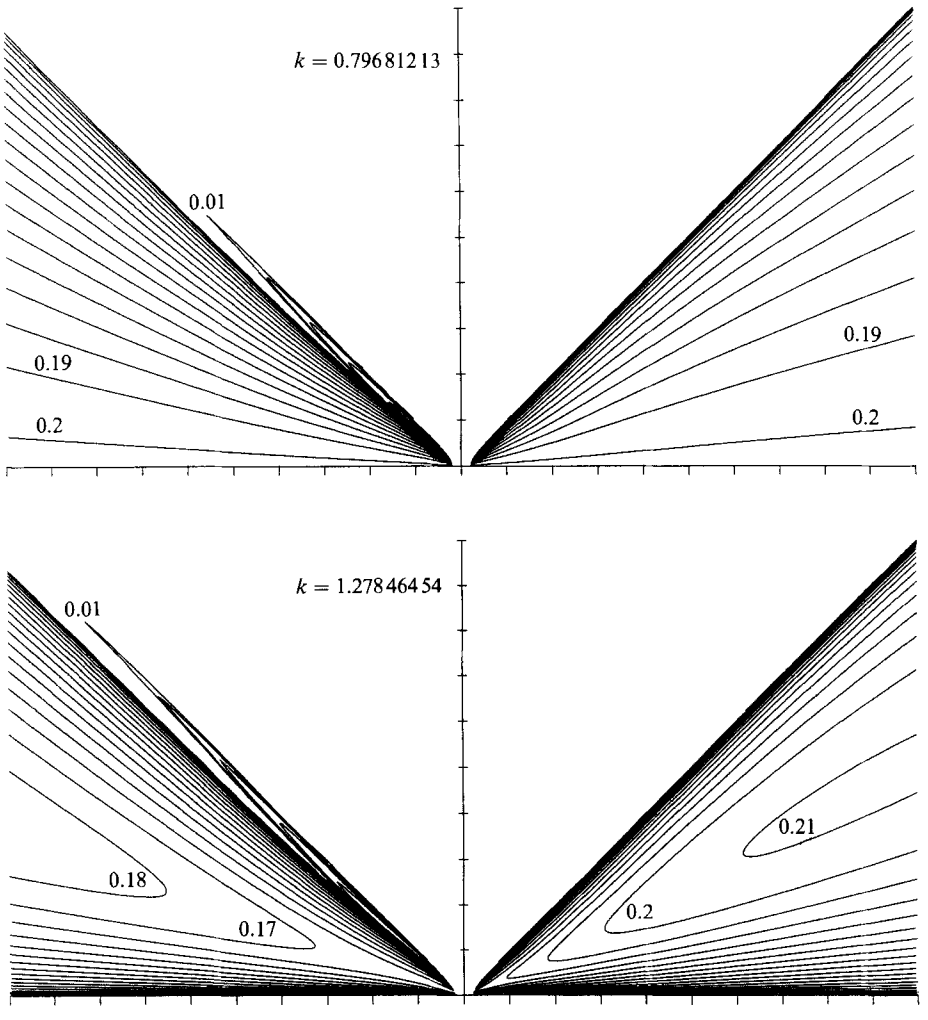

FIGURE 13. For caption see facing page.

the number of nodes varies periodically through $t' \equiv t/2\pi = 100$, the vortex is said to be stable, otherwise it is unstable. In almost all unstable cases, the number of nodes increased by an order of magnitude before the calculation ran out of computer time. This definition of nonlinear stability is not the only one possible, but it serves our purpose by being sensitive to the growth of disturbances that eventually drive the flow continually further from its initially nearly elliptical state. A tighter definition, for example one sensitive to any degree of disturbance amplification, would give very different results (see below).

In figure 15, the results of the 234 calculations are superimposed on the linear stability diagram for $\lambda_0 = 1$, from figure 6. While there is some agreement between the margins of linear and apparent nonlinear stability, it is not perfect. For example, when $\gamma = 0.12$ and $\Omega \geqslant 0$, the case studied in table 1, the linear analysis predicts stability whereas three nonlinear calculations done at different resolutions definitely show fluid-dynamical instability, see figure 16. Given the small size of the initial disturbance in figure 16, no wavenumber having an amplitude in excess of 5×10^{-6},

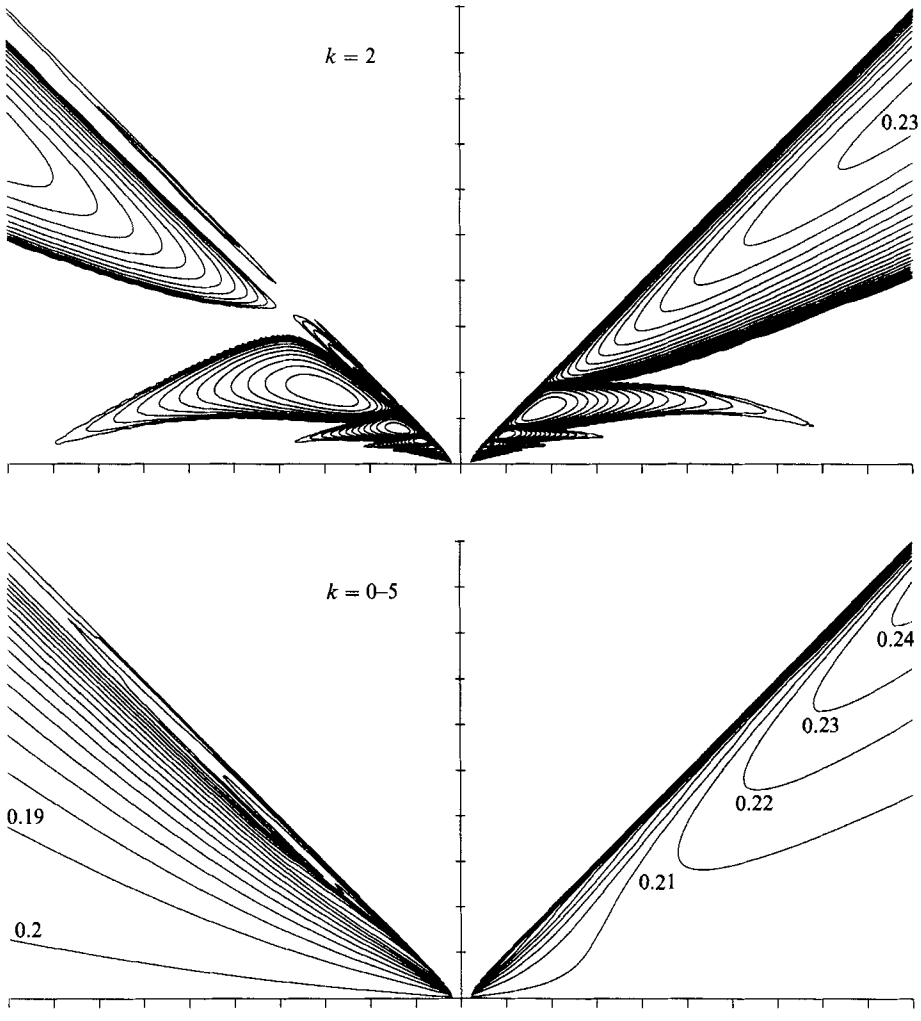

FIGURE 13. Contour maps of growth rate σ when $\lambda_0 = \infty$ for various disturbance wavenumbers k, with the results for $s = +1$ in the left region ($\Omega < 0$) and those for $s = -1$ in the right. Three selected wavenumbers feature, and the final map gives the growth rate maximized over the range $0 \leqslant k \leqslant 5$. A few contours are labelled for clarification.

the observed instability suggests that nonlinear mechanisms, as yet unknown, act to amplify the disturbance no matter how small the initial disturbance may be.

It is notable that, under the right circumstances, an initially circular vortex may be destabilized by strain as weak as 0.008 (at $\Omega = -0.22$). The rate at which the instability destroys the elliptical solution is, however, very slow as figure 17 illustrates. Only a thin filament is pulled from the vortex, yet the vortex will never again recover a simple shape. In this sense, the instability is irreversible. In a coarse-grained sense, the vortex keeps a general elliptical shape, although there remains a noticeable large-scale disturbance. This disturbance may eventually lead to a second filament, then a third, and so on until the vortex either ultimately disappears into a mass of fine filaments or settles down to a vortex of reduced size capable of surviving both the strain forcing and the disturbing influence of the surrounding filaments.

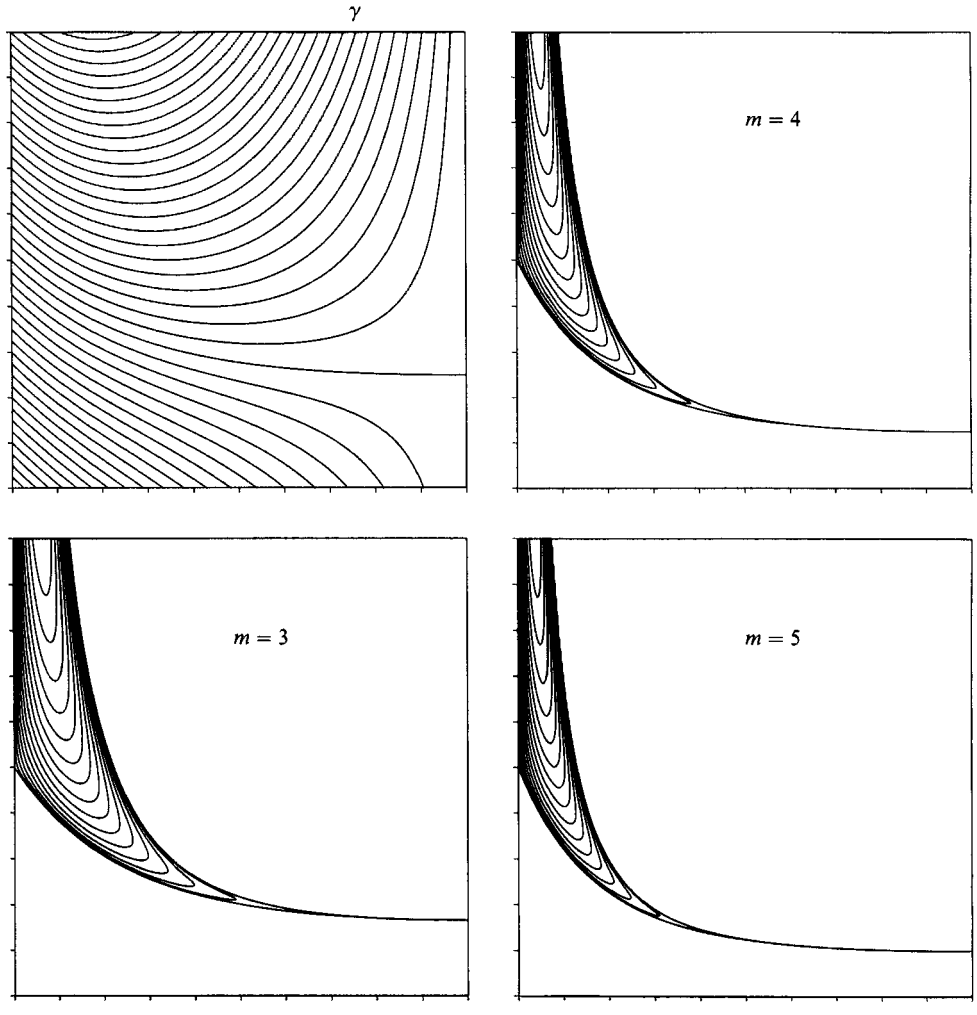

FIGURE 14. Contour maps of the strain rate $\gamma(\Omega, \lambda_0^{-1})$ and the growth rate for $m = 3$, $m = 4$ and $m = 5$ for the stationary solutions. The contour interval is 0.025 in all maps, and the zero-contour is displayed. λ_0^{-1} ranges from 0 to 1, and Ω ranges from $-\frac{1}{2}$ to $\frac{1}{2}$, with tick marks along each axis every 0.1. $\gamma = 0$ along the right-hand edge ($\lambda_0 = 1$) and along the interior curve $\Omega = \Omega_0 = -\lambda_0/(\lambda_0+1)^2$. Along $\Omega = \Omega_0$, the growth rates are identical to those obtained by Love (1893) for a freely rotating elliptical vortex.

By contrast, it takes a comparatively large strain rate to destabilize a vortex when $\Omega > 0$ or when the external rotation is in the same sense as the self-induced vortex rotation (Ω_e). For example, in pure 'cooperative' shear, $\gamma = \Omega$, instability occurs when $\gamma \geqslant 0.475$ (see figure 18); the case $\gamma = 0.475$ is, however, linearly stable. Note the rapid oscillation of the basic flow and the ferocity with which filaments are torn from the vortex. The strong external shear flow sweeps filaments in opposite directions on the upper-left and lower-right sides of the vortex, while the circulating velocity field induced by the vortex eventually draws filaments from one side to the other. So, the filaments whip around the vortex in a highly-eccentric manner.

In the previous two calculations, irreversible changes to the vortex commenced with the loss of a single filament. The next two calculations exhibit other methods

Cosine disturbance			Sine disturbance		
m	δA_m	δB_m	m	δA_m	δB_m
		$\epsilon = 0.002$			
1	0.000 13	0.000 08	1	0.000 01	0.000 52
2	−0.121 24	−0.002 89	2	−0.153 82	0.009 76
3	0.000 53	−0.001 64	3	0.005 74	0.001 13
4	−0.011 23	0.014 80	4	0.025 74	−0.047 38
5	−0.000 58	−0.000 46	5	−0.001 35	0.000 87
6	0.002 43	−0.000 13	6	−0.008 03	−0.002 14
7	0.000 02	0.000 17	7	0.000 66	0.000 20
		$\epsilon = 0.001$			
1	0.000 03	0.000 02	1	—	0.000 13
2	−0.058 37	−0.001 26	2	−0.074 64	0.005 05
3	0.000 15	−0.000 40	3	0.001 43	0.000 25
4	−0.005 69	0.007 39	4	0.012 91	−0.023 64
5	−0.000 13	−0.000 12	5	−0.000 33	0.000 22
6	0.001 20	−0.000 03	6	−0.004 04	−0.001 05
7	0.000 01	0.000 04	7	0.000 17	0.000 04
		$\epsilon = 0.0005$			
1	—	0.000 01	1	—	0.000 04
2	−0.030 37	−0.000 73	2	−0.038 51	0.002 43
3	0.000 03	−0.000 10	3	0.000 37	0.000 07
4	−0.002 83	0.003 69	4	0.006 49	−0.011 82
5	−0.000 04	−0.000 03	5	−0.000 08	0.000 05
6	0.000 60	−0.000 02	6	−0.002 02	−0.000 54
7	—	—	7	0.000 04	0.000 01

TABLE 1. A comparison between linear theory and nonlinear calculations after one period of basic elliptical evolution

Note: Listed in the discrepancy in spectral coefficients δA_m and δB_m between the nonlinear calculations and the linear theory after one period of evolution. The results apply to an initially circular basic vortex in the straining flow $\gamma = 0.12$ and $\Omega = 0$. At the initial instant, the boundary is radially disturbed by the amount $\epsilon \cos 3\theta$ or $\epsilon \sin 3\theta$. In linear theory, after one period ($T = 26.774\,565\,9\ldots$), the vortex boundary changes to $r = 1 + \epsilon(0.516\,411\,8 \cos 3\theta + 0.420\,928\,6 \sin 3\theta)$ for the cosine disturbance and $r = 1 + \epsilon(-0.420\,928\,6 \cos 3\theta + 1.593\,339\,1 \sin 3\theta)$ for the sine disturbance. In the nonlinear calculations, the vortex boundary changes to $r = 1 + \epsilon \Sigma_m A_m \cos m\theta + B_m \sin m\theta$, generally. The results are accurate to the number of decimal places given.

of destabilization. For $\gamma = 0.1$ and $\Omega = -0.3$ (figure 19), two symmetrical filaments are cast from either end of a vortex initially disturbed by random noise only. Just before the filaments appear, the boundary carries a dominant $m = 4$ wave, most clearly seen at $t = 33.5$. The linear analysis also predicts greatest instability for $m = 4$, but several other modes are nearly equally unstable ($\sigma_3 = 0.043$, $\sigma_4 = 0.047$, $\sigma_5 = 0.039$, and $\sigma_6 = 0.015$). For $\gamma = 0.15$ and $\Omega = -0.3$ (figure 20), the boundary carries a complex mixture of waves just preceding the appearance of filaments (the linearly unstable modes amplify at the rates $\sigma_4 = 0.021$, $\sigma_5 = 0.053$, $\sigma_6 = 0.030$, $\sigma_9 = 0.029$, $\sigma_{10} = 0.030$, and $\sigma_{11} = 0.018$). At later times, filaments surround a vortex consumed in large-amplitude breaking waves bent on reducing the vortex to fine filamentary debris.

The next series of calculations begin with elliptical basic vortices, and just those vortices which would be held stationary by the strain field if left undisturbed. By

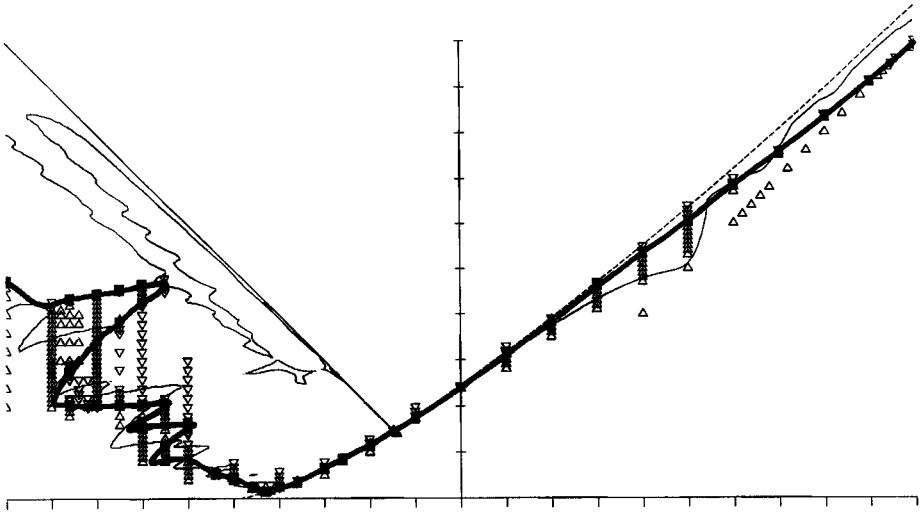

FIGURE 15. Superposition of the results of 234 nonlinear calculations on the linear stability diagram for $\lambda_0 = 1$ (figure 6, $\sigma = 0.01$ contour level only). The symbols $\triangle$ and $\triangledown$ mark the stable and unstable calculations respectively. The heavy solid curve denotes the apparent boundary of nonlinear stability.

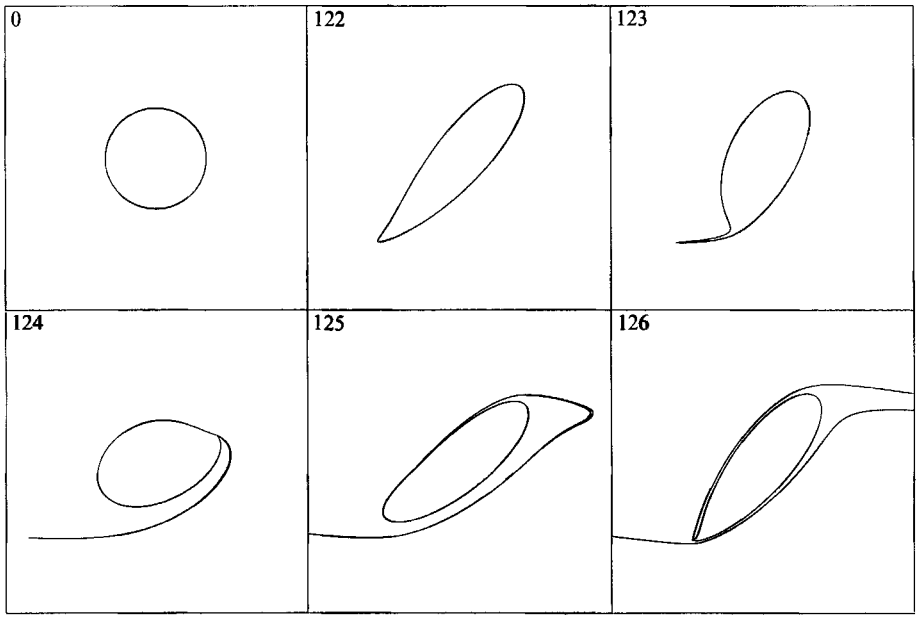

FIGURE 16. A fully nonlinear, contour-surgery calculation of the evolution of a randomly disturbed circular vortex in the straining flow $\gamma = 0.12$, $\Omega = 0$. Time, $t' = t/2\pi$, is labelled in each frame; the evolution proceeds across then down the page. Note the gulf of time between the first two frames; during this interval, the vortex returns to a near circular shape 56 times ($T' = T/2\pi \approx 4.2613$). Algorithm parameters: $\mu = 0.015$, $\delta = 2.81 \times 10^{-5}$, and $\Delta t' = 0.01$. Accuracy: $\epsilon_f = 0.00022$, $\epsilon_A = 0.59°$.

FIGURE 17. (*a*) The evolution of a vortex in the straining flow $\gamma = 0.008$, $\Omega = -0.22$. Here, the vortex returns close to its original circular shape only three times ($T' \approx 31.2715$). $\mu = 0.015$, $\delta = 2.81 \times 10^{-5}$, $\Delta t' = 0.05$, $\epsilon_f = -0.0011$, and $\epsilon_A = 0.33°$. (*b*) A shaded enlargement of the flow at $t = 131$.

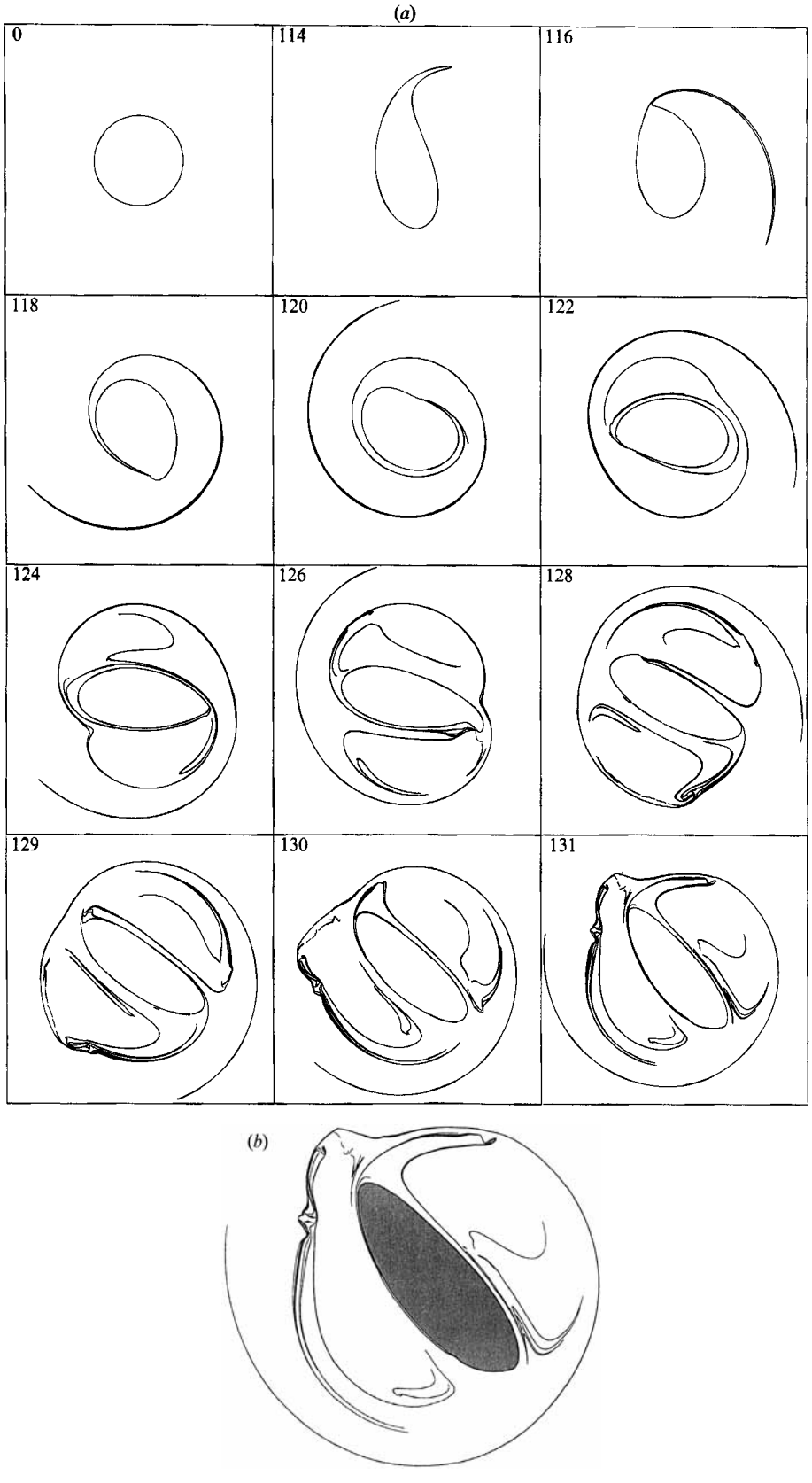

FIGURE 17 (a,b). For caption see facing page.

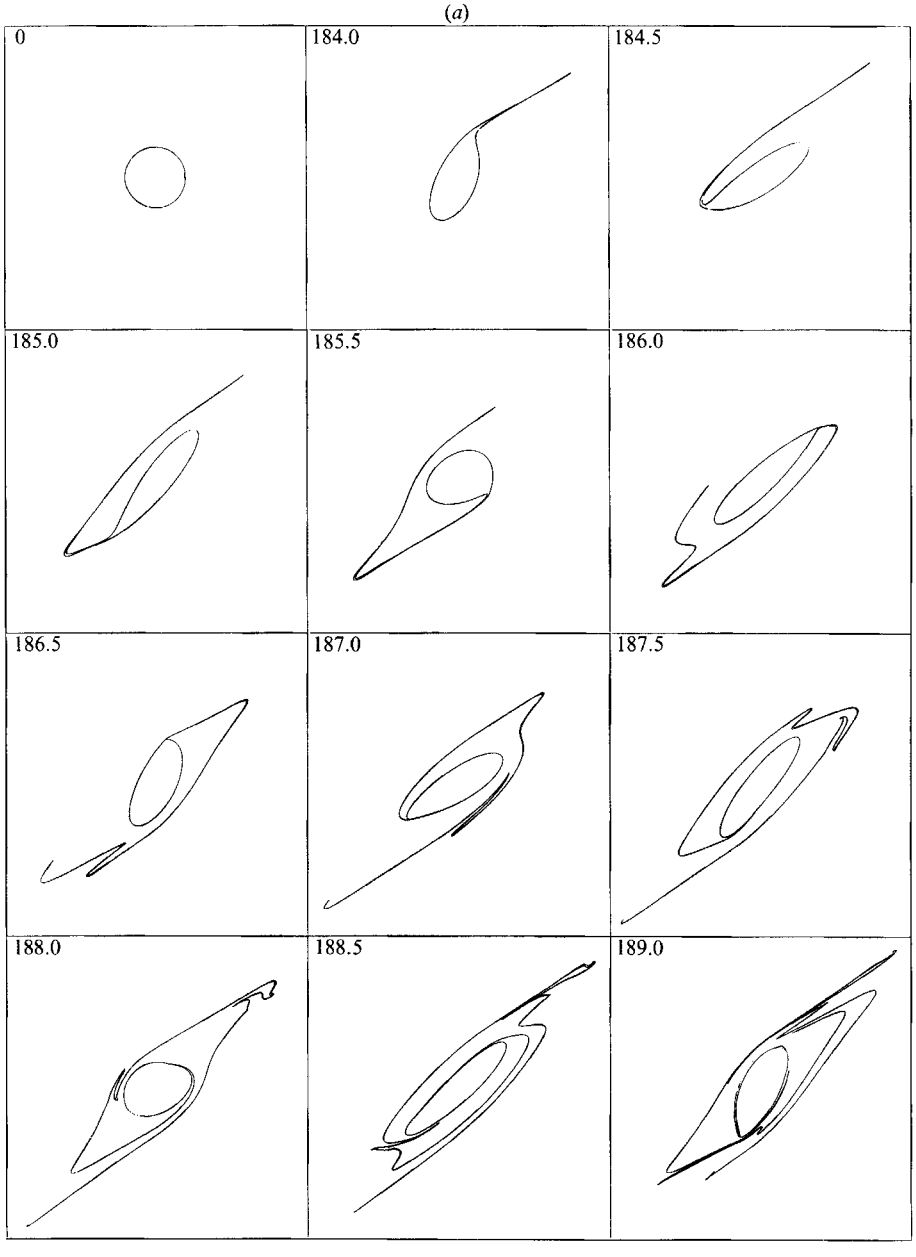

FIGURE 18(a). For caption see facing page.

picking γ and Ω from the ridge of the $m = 3$ instability lobe in figure 14 and varying the aspect ratio λ_0, a transition from recurrent to non-recurrent behaviour was found between $\lambda_0 = 1.7$ and 1.8. In figure 21, for $\lambda_0 = 1.7$ ($\gamma = 0.0369826$ and $\Omega = -0.3093137$), a clear three-fold disturbance emerges, decays back to near zero, and re-emerges after a long period of time. By contrast, in figure 22, for $\lambda_0 = 1.8$ ($\gamma = 0.0391534$ and $\Omega = -0.3037037$), filaments erupt from the vortex boundary and drive the flow further and further from its original state.

The calculations above repeatedly illustrate the generation of small-scale structure

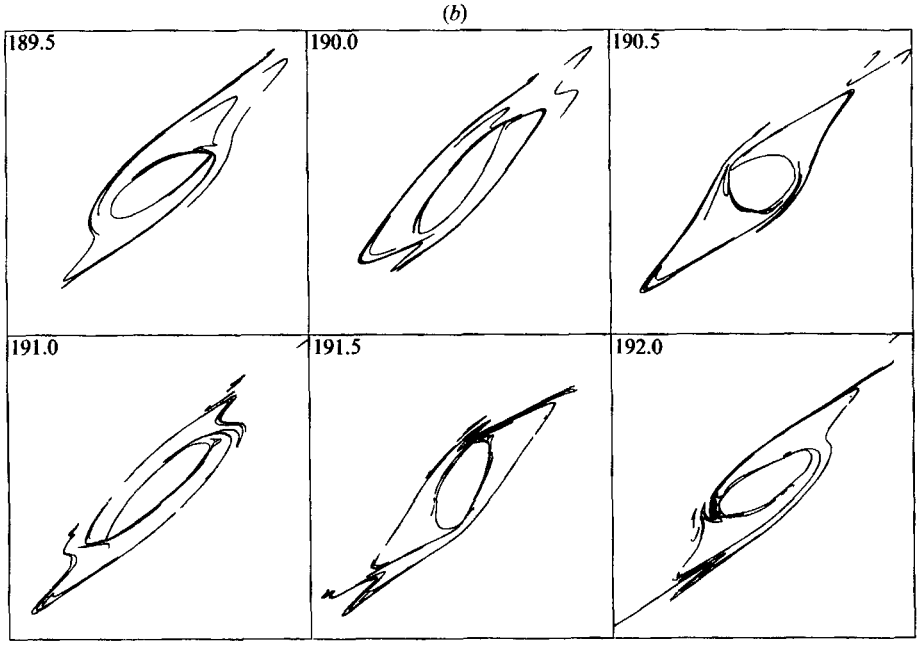

FIGURE 18. (*a*) The evolution of a vortex in the straining flow $\gamma = 0.475$, $\Omega = 0.475$. $T' \approx 1.3346$. $\mu = 0.015$, $\delta = 2.81 \times 10^{-5}$, $\Delta t' = 0.025$, $\epsilon_f = -0.0031$, and $\epsilon_A = 0.90°$. (*b*) Continuation of the evolution shown in (*a*).

(filaments) initially by the breaking of comparatively large-scale waves or disturbances, followed by the interaction of filaments with the remaining, principally large-scale vortex. In figure 22, for example, the original filament thickens along one part of its length owing to the favourable nature of the local strain field (that due to the vortex plus that due to the external flow), and, subsequently, this thickened region approaches the vortex boundary, induces a steepening wave there of the size of the thickened region, and eventually forces new filaments to be shed. This newly disturbed section of the vortex boundary then spreads through repeated 'filamentation' (Dritschel 1988*b*), while other parts of the boundary begin to pass through a similar sequence of events.

5. Discussion

A linear Floquet analysis has revealed a surprisingly rich instability structure for elliptical vortices in an external straining flow. Linear instability extends to arbitrarily weak strain for many values of the strain-axes rotation rate for the reason that the linear-disturbance frequency resonates with harmonics of the basic driving frequency. The growth rates for very weak strain scale with powers of the strain rate and are thus practically negligible. For larger values of the strain rate, growth rates between 5 and 25 % of the relative vorticity of the vortex are frequently encountered. As the minimum aspect ratio λ_0 of the basic solution increases, instability of greater vigour covers a wider range of strain and rotation rates. The first morphological change to the stability diagram with increasing λ_0 occurs at $\lambda_0 = 3$. At this value, the three-fold symmetric eigenmode ($m = 3$) for the unstrained elliptical vortex is marginally stable (Love 1893), and non-zero strain at any permissible value of the

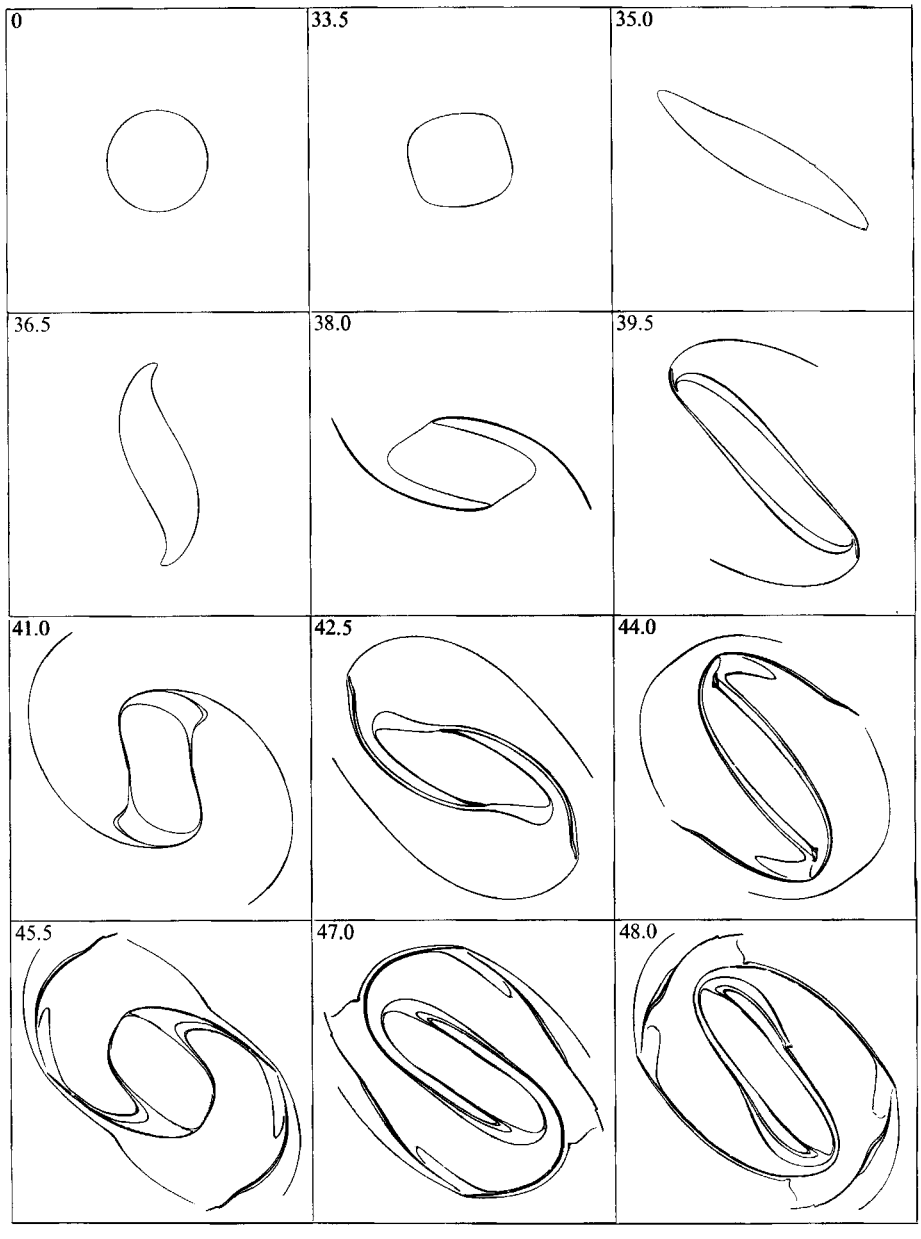

FIGURE 19. The evolution of a vortex in the straining flow $\gamma = 0.1$, $\Omega = -0.3$. $T' \approx 4.1785$. $\mu = 0.015$, $\delta = 2.81 \times 10^{-5}$, $\Delta t' = 0.05$, $\epsilon_f = -0.0028$, and $\epsilon_A = 0.40°$.

rotation rate gives rise to instability. At larger values of λ_0, the $m = 3$ mode is unstable at zero strain, and successively larger m become unstable at both zero and non-zero strain as λ_0 increases. Finally, as $\lambda_0 \to \infty$, new results are obtained for the stability of infinite vortex layers that extend the classical results of Rayleigh (1894). Nearly all values of the strain and rotation rates lead to instability for the layer, but when the strain rate is comparable with the magnitude of the rotation rate, the most unstable disturbance amplifies at a rate an order of magnitude smaller than when the strain is completely absent.

(*a*)

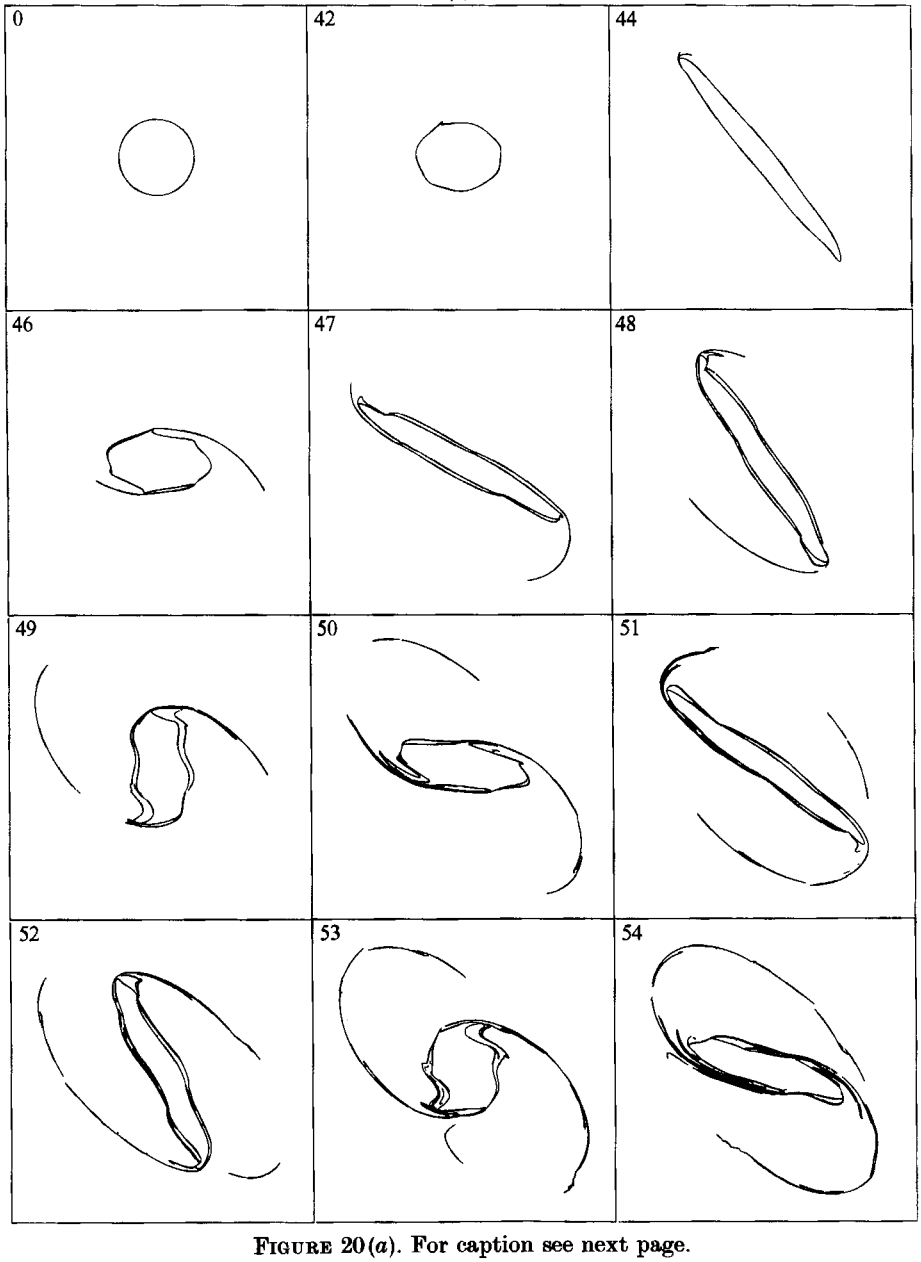

FIGURE 20(*a*). For caption see next page.

Nonlinear simulations on the one hand confirm the linear theory as far as reproducing the linear Floquet matrix with discrepancies that scale with quadratic or cubic powers of the initial disturbance amplitude, yet on the other hand do not always agree with the linear analysis as to the ultimate stability of the flow. The disagreement is on two fronts. First, disturbances to some linearly stable flows definitely do grow, produce filaments, and significantly alter the gross structure of the flow over time, and the evidence presented suggests that a nonlinear mechanism, yet to be determined, can amplify disturbances of any initial size whatever, perhaps initially like some power of t. Second, some linearly unstable flows apparently do not

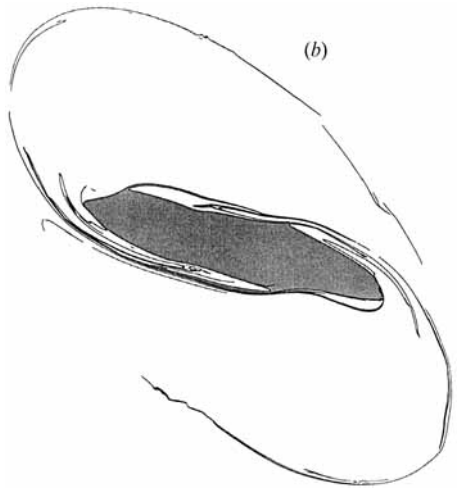

FIGURE 20. (a) The evolution of a vortex in the straining flow $\gamma = 0.15$, $\Omega = -0.3$. $T' \approx 3.8075$. $\mu = 0.015$, $\delta = 2.81 \times 10^{-5}$, $\Delta t' = 0.05$, $\epsilon_f = -0.0016$, and $\epsilon_A = 0.35°$. (b) A shaded enlargement of the flow at $t = 54$.

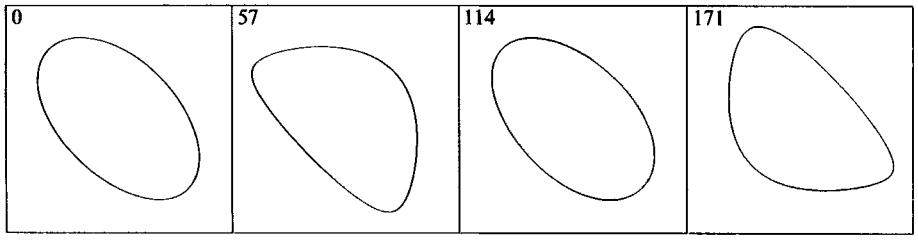

FIGURE 21. The evolution of a vortex of initial aspect ratio $\lambda_0 = 1.7$ in the strain field $\gamma = 0.0369826$ and $\Omega = -0.3093137$. In the absence of disturbances, the vortex would remain stationary. Here small, random disturbances lead to the fully amplified, predominantly three-fold disturbance seen at $t = 57$. This disturbance recurs, after a 180° phase shift, at $t = 3 \times 57 = 171$. $\mu = 0.015$, $\delta = 2.81 \times 10^{-5}$, $\Delta t' = 0.05$, $\epsilon_f = 0.00006$, and $\epsilon_A = 0.29°$.

significantly alter the gross structure of the flow, in the sense that the flow recurrently departs from and returns close to its initial state. That is not to say that the vortex boundary will remain simple for all time, for 'filamentation' may well eventually envelop the whole boundary (Dritschel 1988*b*, 1989*b*), but rather that the coarse-grained position of the vortex boundary may recur over and over again.

The discrepancies found between the linear and nonlinear calculations suggest that a weakly nonlinear theory, developed to cubic order in disturbance amplitude, may be sufficient to explain the origin of the discrepancies. As noted below, such a theory could contribute to the development of a low-order model of two-dimensional vortex dynamics. And, from a mathematical point of view, the theory would no doubt uncover new phenomena, for example, finding large-order behaviour around certain key values of the strain and rotation rate.

A few extended nonlinear calculations have pointed to a generic route to instability. At first, a disturbance amplifies at the expense of the basic, periodic flow (see the Appendix for a discussion of the energetics). Next, the disturbance steepens or begins to tilt to one side. Steepening is fundamentally a nonlinear process linked with the growth of large wavenumbers at the expense of smaller ones. By analogy

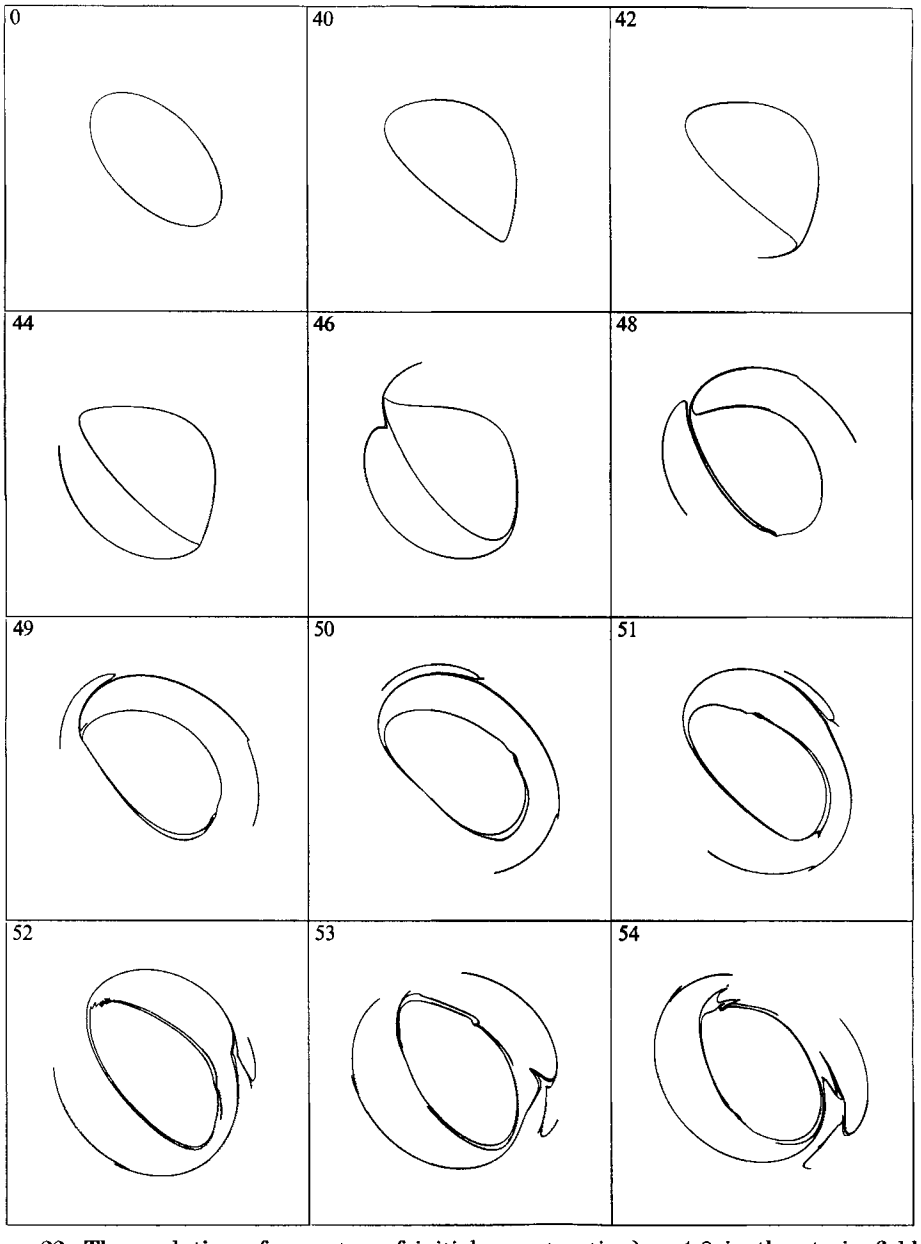

FIGURE 22. The evolution of a vortex of initial aspect ratio $\lambda_0 = 1.8$ in the strain field $\gamma = 0.0391534$ and $\Omega = -0.3037037$. As in the previous figure, the strain field is such as to keep an undisturbed vortex of this aspect ratio stationary. Note the complex motion of the filaments and, in particular, the way in which enlarged parts of the filaments approach and dig into the vortex boundary. $\mu = 0.015$, $\delta = 2.81 \times 10^{-5}$, $\Delta t' = 0.05$, $\epsilon_f = -0.00021$, and $\epsilon_A = 0.042°$.

with previous work (Dritschel 1988*b*, 1989*b*), steepening takes place where fluid particles on the vortex boundary are converging, usually to one side of the disturbance maximum. An abrupt change then occurs when the disturbance folds over or 'breaks', at which stage filaments begin to form. The contour perimeter then rapidly grows as the filaments are thinned and stretched by the straining flow arising from both the external flow and the vortex itself. Subsequently, the straining flow

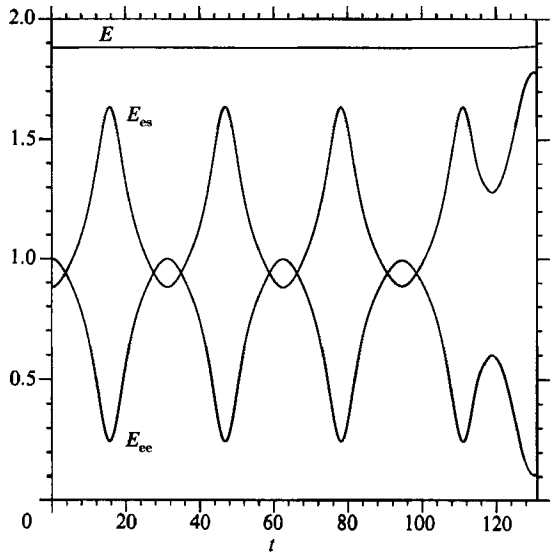

FIGURE 23. The time evolution of the vortex self-energy E_{ee}, the interaction energy between the vortex and the strain flow E_{es}, and the combined, theoretically invariant excess energy E for the unstable vortex evolution depicted in figure 17.

largely governs the motion of the filaments, the filaments moving about as if they were passive. But, the straining flow around the vortex is not wholly extensional, that is, filaments are not always being thinned and stretched everywhere. At times, parts of filaments may be sufficiently enlarged to induce further filament generation along the vortex boundary. And, all along, new disturbances are swelling up, steepening, and generating further filaments, further fuelling the spiralling complexity of the vortex boundary and the deterioration of the interior vortex core.

A challenging problem would be to relax the assumption of steady strain and rotation rate, for these are the worst assumptions of all in a fluid with many interacting vortices. But one can still study the evolution of linear disturbances using the equations developed in §3, for these equations apply equally well to unsteady γ and Ω. An exciting possibility would be to combine the 'elliptical moment model' of Melander *et al.* (1986) with the linear disturbance equations developed here, or better yet, with a future weakly nonlinear set of equations. Melander *et al.* (1986) have derived an approximate set of evolution equations for the aspect ratio, orientation, and centroid position of any number of interacting, separated vortices. Essentially, they extended, non-trivially, Kida's (1981) analysis to more than one vortex by explicitly calculating the strain field arising from all the vortices. A model of vortex dynamics substantially simpler than the full equations and less restrictive than the moment model is envisioned which combines (*a*) the moment model, (*b*) disturbance equations, and (*c*) a means to introduce disturbances, to merge vortices, and to approximate the mean effects of fine-scale structure. Disturbances can be introduced by evaluating the higher-order moments discussed by Melander *et al.* (1986). Results from current research on the merging of vortices in an external strain flow are providing quantitative estimates for the completeness of merging and may lead to a simple, approximate procedure for it. Efforts are also being directed at tackling perhaps the most difficult problem, namely to capture the gross effects of the unresolved, fine-scale features in coarse-resolution calculations, by the development

of 'fuzzy-contour dynamics', an approximate model for the evolution of steep-, but finitely steep-edged vortices (in preparation).

The computations were performed on the Cyber 205 at the University of Manchester Computer Centre and on the Cray X-MP/48 at Rutherford-Appleton Laboratory, with the support of the UK Science and Engineering Research Council, the US Office of Naval Research, and the Natural Environmental Research Council's UK Universities' Global Atmospheric Modelling Project.

Appendix. The energy of a straining flow

Suppose that there exists a finite region of the plane where the vorticity differs from that of the background straining flow -2Ω. While the energy, the kinetic energy, is generally infinite, one can remove the infinite parts of the energy to leave a finite, invariant quantity called the 'excess energy'. The procedure to remove the infinite parts closely follows that discussed in an earlier work (Dritschel 1985), in which the excess energy for an unstrained flow was defined.

Basically, one separates the energy

$$T = \frac{1}{2}\iint (u^2+v^2)\,\mathrm{d}x\,\mathrm{d}y, \tag{A 1}$$

where

$$u = u_\mathrm{e}+\gamma x-\Omega y, \quad v = v_\mathrm{e}-\gamma y+\Omega x \tag{A 2a, b}$$

into three terms, all of which are generally infinite:

$$T_\mathrm{ee} = \frac{1}{2}\iint (u_\mathrm{e}^2+v_\mathrm{e}^2)\,\mathrm{d}x\,\mathrm{d}y, \tag{A 3a}$$

$$T_\mathrm{es} = \gamma\iint (xu_\mathrm{e}-yv_\mathrm{e})\,\mathrm{d}x\,\mathrm{d}y+\Omega\iint (xv_\mathrm{e}-yu_\mathrm{e})\,\mathrm{d}x\,\mathrm{d}y, \tag{A 3b}$$

$$T_\mathrm{ss} = \tfrac{1}{2}(\gamma^2+\Omega^2)\iint (x^2+y^2)\,\mathrm{d}x\,\mathrm{d}y-2\gamma\Omega\iint xy\,\mathrm{d}x\,\mathrm{d}y. \tag{A 3c}$$

One then removes the parts of these terms that depend only on the size of the domain, say L, as $L\to\infty$ and on the total, finite, invariant circulation Γ_e associated with the relative vorticity distribution ω_e ($u_\mathrm{e} = -\partial\psi_\mathrm{e}/\partial y$, $v_\mathrm{e} = \partial\psi_\mathrm{e}/\partial x$, $\omega_\mathrm{e} = \nabla^2\psi_\mathrm{e}$). The term T_ss can be removed entirely as it depends only on the size of the domain. The infinite parts of T_ee and T_es can be removed by an integration by parts and an application of Stokes' theorem leaving

$$T^*_\mathrm{ee} = -\frac{1}{2}\iint \omega_\mathrm{e}\psi_\mathrm{e}\,\mathrm{d}x\,\mathrm{d}y, \tag{A 4a}$$

$$T^*_\mathrm{es} = \gamma\iint \omega_\mathrm{e}xy\,\mathrm{d}x\,\mathrm{d}y-\tfrac{1}{2}\Omega\iint \omega_\mathrm{e}(x^2+y^2)\,\mathrm{d}x\,\mathrm{d}y. \tag{A 4b}$$

The invariant, finite part of the energy is simply $T^* = T^*_\mathrm{ee}+T^*_\mathrm{es}$, the sum of the self-energy and the energy arising from the interaction between the external flow and the anomalous flow $\boldsymbol{u}_\mathrm{e}$.

In this form, the excess energy T^* cannot be used to compare the energetics of different vorticity configurations, because the stream function ψ_e in (A 4a) is known

only to within a constant. To resolve this ambiguity, the stream function is defined as

$$\psi_e = \frac{1}{2\pi}\iint \omega_e(x', y') \log\left[|\boldsymbol{x} - \boldsymbol{x}'|/l\right] \mathrm{d}x' \, \mathrm{d}y' \tag{A 5}$$

where l is an appropriate lengthscale (Dritschel 1985). While there is some freedom of choice, l must be chosen in terms of invariant quantities (not including T^* of course). In a straining flow, the only available invariant quantities are the areas enclosed within isovortical contours (ω_e = constant) or within contours of discontinuous vorticity, depending on whether the vorticity distribution is continuous or piecewise-constant. Contour area must then appear in the definition for l, and it is suggested that the following choice be adopted to standardize the definition of excess energy:

$$\pi l^2 = \frac{1}{\omega_{\max} - \omega_{\min}} \int_{\omega_{\min}}^{\omega_{\max}} A(\omega) \, \mathrm{d}\omega \tag{A 6}$$

for continuous vorticity distributions, and

$$\pi l^2 = \frac{1}{\omega_{\max} - \omega_{\min}} \sum_{k=1}^{N} A_k |\tilde{\omega}_k| \tag{A 7}$$

for piecewise-constant ones. Here, $\omega_{\max}$ is the maximum value of ω_e, and likewise $\omega_{\min}$ is the minimum value. The sum in (A 7) ranges over the number of contours, and $|\tilde{\omega}_k|$ is the jump in vorticity across the kth contour. For a single vortex patch, πl^2 is simply the vortex area A.

The energetics of the undisturbed and disturbed elliptical vortices of this paper illustrates the important interplay between the vortex self-energy and the vortex–strain field interaction energy. Defining $E = 16\pi T^*/A^2 + 4\Omega$ as a dimensionless energy, the undisturbed elliptical vortices satisfy

$$E = 1 - 2\log\frac{(\lambda_0+1)^2}{4\lambda_0} + 2\gamma\frac{\lambda_0^2 - 1}{\lambda_0} - 2\Omega\frac{(\lambda_0 - 1)^2}{\lambda_0}$$

or $E = 1 + 2c$, where c is the constant of integration appearing in (3). The terms proportional to γ and Ω together comprise the interaction energy. In general, the interaction energy rises and falls, being exactly compensated by the fall and rise of the vortex self-energy. Of greater interest, though, is the variation of these components of the energy in an unstable flow. Figure 23 shows the time evolution of the self-energy, $E_{ee} = 16\pi T^*_{ee}/A^2$, the interaction energy, $E_{es} = 16\pi T^*_{es}/A^2 + 4\Omega$, and the combined, theoretically invariant energy E for the calculation illustrated in figure 17 ($\lambda_0 = 1$, $\gamma = 0.008$, and $\Omega = -0.22$; for notes on the numerical calculation of E, see Dritschel 1986, 1989*b*). E changes by only 0.1% during the entire evolution. E_{ee} and E_{es} oscillate at first, but once the instability becomes noticeable in figure 17, E_{es} increases beyond its normal range at the expense of E_{ee}. In other words, the instability corresponds to a transfer of energy from the vortex self-energy to the vortex–strain field interaction energy.

REFERENCES

Abramowitz, M. & Stegun, I. A. 1965 *Handbook of Mathematical Functions*. Dover.

Basdevant, C., Legras, B. & Sadourny, R. 1981 A study of barotropic model flows: intermittency, waves and predictability. *J. Atmos. Sci.* **38**, 2305–2326.

DRITSCHEL, D. G. 1985 The stability and energetics of corotating uniform vortices. *J. Fluid Mech.* **157**, 95–134.

DRITSCHEL, D. G. 1986 The nonlinear evolution of rotating configurations of uniform vorticity. *J. Fluid Mech.* **172**, 157–182.

DRITSCHEL, D. G. 1988*a* Contour surgery: a topological reconnection scheme for extended integrations using contour dynamics. *J. Comput. Phys.* **77**, 240–266.

DRITSCHEL, D. G. 1988*b* The repeated filamentation of two-dimensional vorticity interfaces. *J. Fluid Mech.* **194**, 511–547.

DRITSCHEL, D. G. 1989*a* On the stabilization of a two-dimensional vortex strip by adverse shear. *J. Fluid Mech.* **206**, 193–221.

DRITSCHEL, D. G. 1989*b* Contour dynamics and contour surgery: numerical algorithms for extended, high-resolution modelling of vortex dynamics in two-dimensional, inviscid, incompressible flows. *Computer Phys. Rep.* **10**, 77–146.

FORNBERG, B. 1977 A numerical study of 2-D turbulence. *J. Comput. Phys.* **25**, 1–31.

KIDA, S. 1981 Motion of an elliptic vortex in a uniform shear flow. *J. Phys. Soc. Japan* **50**, 3517–3520.

LEGRAS, B. & DRITSCHEL, D. G. 1989 Vortex stripping. *J. Fluid Mech.* (submitted). (See also: Dritschel, D. G. 1989 In *Mathematical Aspects of Vortex Dynamics* (ed. R. E. Caflisch). Society for Industrial and Applied Mathematics.)

LEGRAS, B., SANTANGELO, P. & BENZI, R. 1988 High resolution numerical experiments for forced two-dimensional turbulence. *Europhys. Lett.* **5**, 37–42.

LOVE, A. E. H. 1893 On the stability of certain vortex motions. *Proc. Lond. Math. Soc.* **25**, 18–34.

MCWILLIAMS, J. C. 1984 The emergence of isolated coherent vortices in turbulent flow. *J. Fluid Mech.* **146**, 21–43.

MELANDER, M. V., ZABUSKY, N. J. & STYCZEK, A. S. 1986 A moment model for vortex interactions of the two-dimensional Euler equations. Part 1. Computational validation of a Hamiltonian elliptical representation. *J. Fluid Mech.* **167**, 95–115.

MOORE, D. W. & SAFFMAN, P. G. 1971 The structure of a line vortex in an imposed strain. In *Aircraft Wake Turbulence and its Detection* (ed. J. Olsen, A. Goldberg & N. Rogers). Plenum.

RAYLEIGH, LORD 1894 *The Theory of Sound*, 2nd edn. Macmillan (see also: 3rd edn, 1945).

ZABUSKY, N. J., HUGHES, M. H. & ROBERTS, K. V. 1979 Contour dynamics for the Euler equations in two dimensions. *J. Comput. Phys.* **30**, 96–106.